http://dx.doi.org/10.1016/j.apenergy.2023.121122

Simulation and experimental study on the energy performance of a pre-fabricated photovoltaic pavement

Yijie Zhang[1*], Tao Ma[2*], Hongxing Yang[1], Zongyu Li[3], Yuhong Wang[3]

[1]Renewable Energy Research Group (RERG), Department of Building Environment and Energy Engineering, The Hong Kong Polytechnic University, Hong Kong, China

[2]Engineering Research Centre of Solar Energy and Refrigeration of MOE, School of Mechanical Engineering, Shanghai Jiao Tong University, Shanghai, China

[3]Department of Civil and Environmental Engineering, The Hong Kong Polytechnic University, Hong Kong, China

Corresponding authors: tao.ma@sjtu.edu.cn (Tao Ma); yijie-sucy.zhang@connect.polyu.hk (Yijie Zhang)

Abstract

Photovoltaic pavement (PVP) is an emerging technology to harvest solar energy from roads, which could use the limited urban area renewable energy production, especially under the carbon neutrality targets. This study proposes a thermal-electrical mathematical model for a PVP system based on the Finite Difference method on heat nodes and a 5-parameter I-V curve model. An outdoor test is conducted for model validation, showing 1.68% and 3.60% mean absolute errors for PV cell temperature and output. Lab tests and road anti-skid property tests are also conducted. The experiment results show that the PV output on a sunny day could reach 0.68 kWh/m^2, with electrical power generation efficiency of 14.71%. Based on the proposed model, two cases, in Hong Kong and Shanghai, are analyzed for an entire year. The parametric analyses recommend epoxy resin filling instead of air filling, with the annual maximum PVP module surface temperature reduction at 8.6% (Shanghai) and 8.4% (Hong Kong). The influence of road surface materials and asphalt concrete depth variation are also discussed. Besides the obvious heat island effect alleviation in Summer found from the surface temperature decrease, the snow melting potential in Winter could also be found with the increase of minimum surface temperature by 1.02℃ (Shanghai). Moreover, the potential of PVP application is also analyzed for 255 Chinese cities with seasonal variations, demonstrating the heat and electrical performances with seasonal average results, with maximum average road surface temperature reduction at -4.18℃ in summer and maximum increase, e.g., for Beijing up to 3.36℃ in Winter. The cities in the west and northeast China are shown with higher PVP generation potential.

Keywords: Photovoltaic pavement, experimental study, thermal nodal, energy analysis, heat island effect, application potential

Nomenclature

I	Current (A)
A	Area for PV panel (m^2)
a	Thermal diffusivity (m^2/s)
c	Specific heat capacity (J/kg/K)
E	Energy (kWh)

E_g	Band gap
G	Solar irradiation (W/m^2)
h	Convective heat transfer coefficient (W/m^2/℃)
I_m	PV output current at maximum power point (A)
i	Value in the x axis for the thermal node
j	Value in the y axis for the thermal node
N	Cell number in PV panel
K	Temperature coefficient (%/℃)
k	Thermal conductivity (W/m/K)
P	Power (W)
Q	Heat flux (W/m^2)
q	Electron charge, 1.602×10^{-19} (C)
R	Resistance (Ω)
T	Temperature (℃)
t	Time (s)
Δt	Time step, 30 (s)
V	Voltage (V)
V_m	PV output voltage at maximum power point (V)
v_{win}	Wind velocity (m/s)
α	Absorptivity
ε	Emissivity
η	PV electricity efficiency
σ	Stefan-Boltzmann constant, at 5.67×10^{-8}W/m^2/K^4
ρ	Density (kg/m^3)
τ	Transmissivity

Subscripts

0	Saturation diode current (A)
a	Ambient air environment (℃)
cell	PV cell
g	glass
gd	ground
i	Current
ini	Initial value

pa	Parallel
pc	Photocurrent (A)
pv	Photovoltaic
pvs	PV surface
se	series
sky	Equivalent sky temperature (℃)
t	Thermal
v	Voltage

Superscripts

p	Numerical simulation time sequence

Abbreviations

ADDM	Alternative direction difference method
BPN	British Pendulum number
BPT	British Pendulum Tester
E(I)FDM	Explicit (Implicit) finite difference method
HK	Hong Kong
MAE	Mean absolute error
NOCT	Normal operating cell temperature (℃)
PIPVT	PV integrated photovoltaic thermal
PV	Photovoltaic
PVP	Photovoltaic pavement
RMSE	Root mean square error
SH	Shanghai
STC	Standard testing condition

1 Introduction

The carbon neutrality targets accelerate renewable energy installation, especially photovoltaic (PV) technology [1-3]. The PV installation rate increased rapidly from 101.7GWp (2012) to 843.1GWp (2021) globally, and proportion of China takes up about 36.3% of the PV installation capacity in 2021, as reported by IEA [4]. However, the further increase of PV installation in the urban area is challenging, e.g., to increase solar energy application in HK to take up 1-2% of energy production by 2050 [5], with so little spatial area for PV installation in the metropolis. Besides the rooftop and façade PV of the buildings in the city, the PV installation integrated into the transportation road is gradually paid more attention to. The road area takes up a sufficient proportion of the space, e.g.,

around 55 km/100km^2 in China in 2021 [6] and 30-45% in Chicago [7]. It may provide the installation opportunity for PV panels due to the low use rate during daytime.

To harvest solar energy from the road is an emerging topic, with most studies in the last 5 years. Traditionally the off-grid PV system is installed on the telegraph pole beside the roadway [8]. However, nowadays, the integration of PV panels directly into the roadways provides electricity not only for road lightening, but the basic sensors and controllers for smart transportation basis as well [9]. As a renewable electricity supplier, the PV roadway could also be integrated into the distributed energy system application for the smart grid, like EV wireless charging [10] and provide applicable situation for next generation PV cell with novel coatings [11, 12]. Besides the electricity gain, heat island mitigation in the urban areas is also an attractive advantage of PV roadway installation [13, 14], with heat application potential like snow melting [15]. Like the PV tiles, the PV roadway module could also provide other advantages like piezoelectric and thermoelectric energy harvesting [16], when integrating with the conventional asphalt concrete road layer.

The integration of PV cell with the roadway includes different kinds of roadways and have different terms defined in the studies, from Photovoltaic pavement (PVP) [7, 17], PV road [8], PV sideway, PV canopy [18], solar pavement [19-22], solar road [9], PV floor tile [23] to e-Road [24]. To depict the PV panel in a more acknowledged way, the PVP or solar pavement is recommended. For better practical use, the modular production [25] of the pre-fabricated PVP module is applied to this study.

Several PV road projects emerged at the beginning of this field, such as the 2013 Netherland solar bike path and walkable solar PVP in Spanish by the company Onyx Solar mentioned in our previous work [26]. However, the problems are gradually found in the short end of those projects, including the slippery surface [27], low electricity efficiency [28], and weak structure [21]. Correspondingly, the studies on solar pavement deal with the practical difficulties from electricity, thermal and structural aspects with outside factors like climate, traffic, environment, socioeconomic benefit, and technology readiness level [29].

The electrical installation is reduced for easy installation and higher structural loading capacity, varying from 120Wh to 460Wh per m^2, as concluded by Vizzarl et al. [30] in 2021. A self-compacting concrete hollow slab PVP is studied for power generation and structural simulation by Zha et al. [31]. At the same time, the technical performances were simulated by PVsyst software, which does not consider the impact of ground and the apparent PV cell temperature increase. Based on the previous studies in Dr. Ma's group [27, 32], the pavement integrated PV module utilizes the simple PV generation model which only considers the temperature influence on PV efficiency and simply regards the ground boundary condition as adiabatic. Also, the horizontal heat transfer in the width direction is neglected [33]. As for the electrical model, the PV 5-parameter model is introduced to the PV pavement module simulation [26]; however, the heat transfer is neglected, and the correspondingly thermal-electrical model is lacking. In the studies conducted by Xiang et al. in 2020 [34] and 2021 [35, 36], the ground influence is considered in the heat transfer model, however, the electrical model and thermal model are not integrated, and the PV generation calculation is simple by the PV efficiency variation based on temperature coefficient.

Another key point on the PVP module is the urban heat island effect reduction. The urban heat island alleviation is achieved by a 3-5℃ temperature decrease in pavement in summer by Xie and Wang [14]. Similarly, the heat dissipation of the PVP module is shown obviously in the experiments

conducted by Zhou et al. [37] and Efthymiou et al. [7]. However, the experiment is rough without consideration of the thick ground heat transfer effect. These studies usually select the road type with asphalt or asphalt concrete with fixed depth. The other work conducted by Zhou and his colleagues [38, 39] focus on the PVP and PIPVT module structure performances. The structure design of the PVP module is also a significant focuses with studies on novel encapsulant module architecture [40], self-compacting concrete [31], addition of a vapor chamber, water tank and shading board [13], hollow structure with water pipes [37], and a mixture of fine concrete (cement and fine aggregate such as sand) and optical fiber [25]. The tempered glass with a metal frame and damp layer shows good loading performance and lower cost, which is recommended [26].

There are also some other considerations regarding the future application of PVP [22], such as street signaling, street lights [41], autonomous driving guide, and wireless charging integration [24]. However, most of them are far from practical use and will be future considerations in the academia. The economic considerations emerge with the maturity of this technology [42, 43] as well.

Based on the studies mentioned above on PVP modules, several problems still exist in the research field of PV road module research, which originated in recent decades. Firstly, the traditional NOCT model to simulate the PV cell temperature may not be applicable to the PV road module, for it is embedded into the roadway or sidewalk in the ground. The ground impact is neglected or assumed as an adiabatic boundary condition in the heat resistance model in the previous studies. Moreover, the simple PV electrical generation model, simply considering temperature coefficient, is the mostly used PV model, while it is of relatively low accuracy. Besides, the experimental studies for the PV road module from different aspects are still lacking at this stage, for the PV road module is a novel application of PV module. Furthermore, the long-term performance evaluations of different cities are also rarely found in previous studies, especially with both PV generation potential and PV cell temperature. Also, the cost analysis of the PVP module and the vehicle shading influence are crucial concerns but rarely discussed.

For the PV road further study with higher model accuracy and reliable experiments, this study aims to provide a solid study on PVP module integrated thermal and electrical performances with both numerical and experimental studies. The major contributions and novelties could be concluded as follows: (1) An electrical-thermal mathematical model is established for a prefabricated PV road module with consideration of ground impact, which is of high accuracy with model verification. (2) Lab test and outdoor experiments have been conducted for the module electrical and thermal features, and anti-skid performances. (3) Parametric analyses of different backfilling and surrounding ground materials on module thermal performance have been conducted for module design optimization. (4) The annual energy output and road surface temperature of different cities in China, especially Hong Kong and Shanghai, have been compared with seasonal variations to provide PVP module potential reference nationwide. (5) Economic considerations and partial shading influence have been discussed in detail with relative modelling and experiments.

2 Background and system description

The PV-road module is simulated and produced for a 10m-long PV road demonstration project at Sha Tin in Hong Kong. The lab and outdoor experimental tests are conducted at this stage. Fig. 1 displays the system demonstration figure and real project photo. The PV pavement is designed for the roadway, with one manufactured model shown from the top view. Four Pt100 sensors are sticked to the rear

glass of the mono-silicon PV cell. Nine PV cells are cut in half and connected in one series for low system current in practical conditions. The area of the entire pre-fabricated module is 0.25m^2 with the installation power at 31.5Wp. Thus, the electrical installation of the whole system is 126Wp/m^2, which is relatively high compared to the product from Solar Roadways at 97.3W/m^2 with an efficiency of 11.2% [28]. More specifications can be found in Table 1.

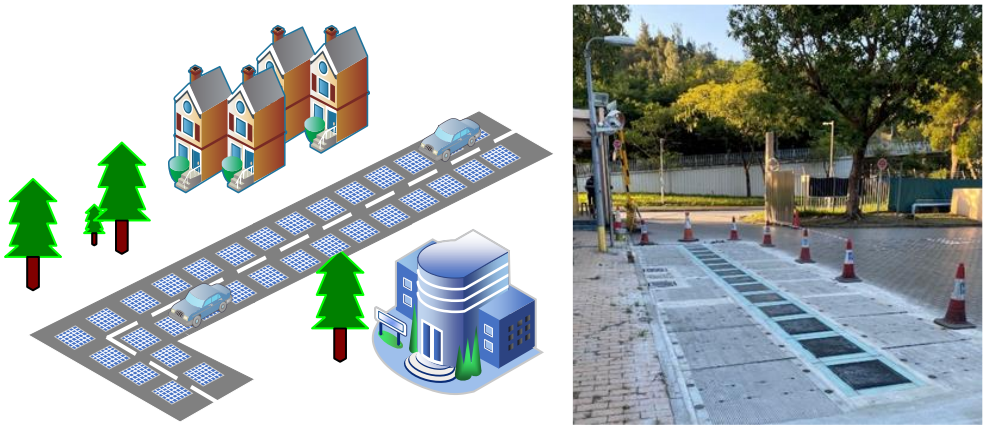

(a) (b)

Fig. 1 PV pavement: (a) demonstration diagram; (b) the real project.

The layout of the PVP module in this study and the ground layers are shown in Fig. 2. The front and rear sides of the PV cell use the tempered glass sheet for higher structural strength and better protection [17, 37, 38]. The patterns are added to the front surface of the module for higher anti-skid properties compared to the resin. The damp layer with backfilling materials of air and epoxy resin (EP) is used instead of the hollow structure [27, 33] for better support. The entire module prefabricates the metal frame, and is designed to be embedded into the roadway with ground materials. The three layers, including surface ground layer, base/subbase and subgrade [37] are considered to better analyze the ground influence. The surface ground layer is selected as asphalt-concrete, which is mostly used in the urban area at 120mm, within the range of 30 -120mm, according to the previous studies [14, 32, 36, 37, 44]. The parametric analysis of the layer depth can be found in Appendix. The base (integration of base and subbase) depth selects 360mm in the range of 360 [45] to 450mm [14]. The subgrade is selected at more than 3500mm to provide a more accurate analysis, which could be found at more than 2000mm [14].

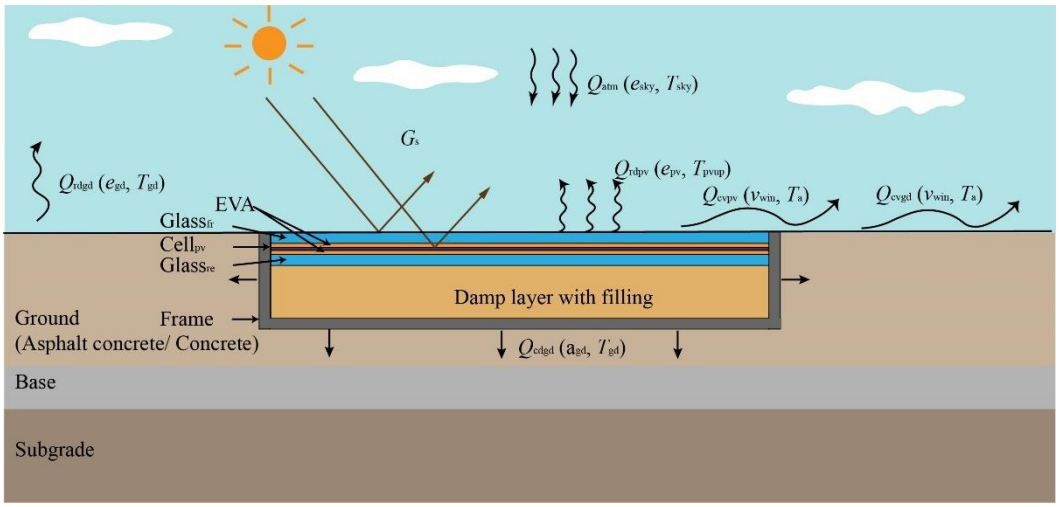

Fig. 2 Systematic diagram of the PV road module

3 Modelling and simulation

The overall methodology for this study is shown in Fig. 3. The data inputs include information and parameters from weather, site, PV module, material, and market. The thermal-electrical PV generation model is based on the PV cell temperature via a heat balance equation. Both lab and outdoor tests are conducted to collect crucial module data and verify the proposed thermal-electrical model. The long-term analysis of different cities in China has been conducted with considerations of PV road module surface temperature and electrical generation.

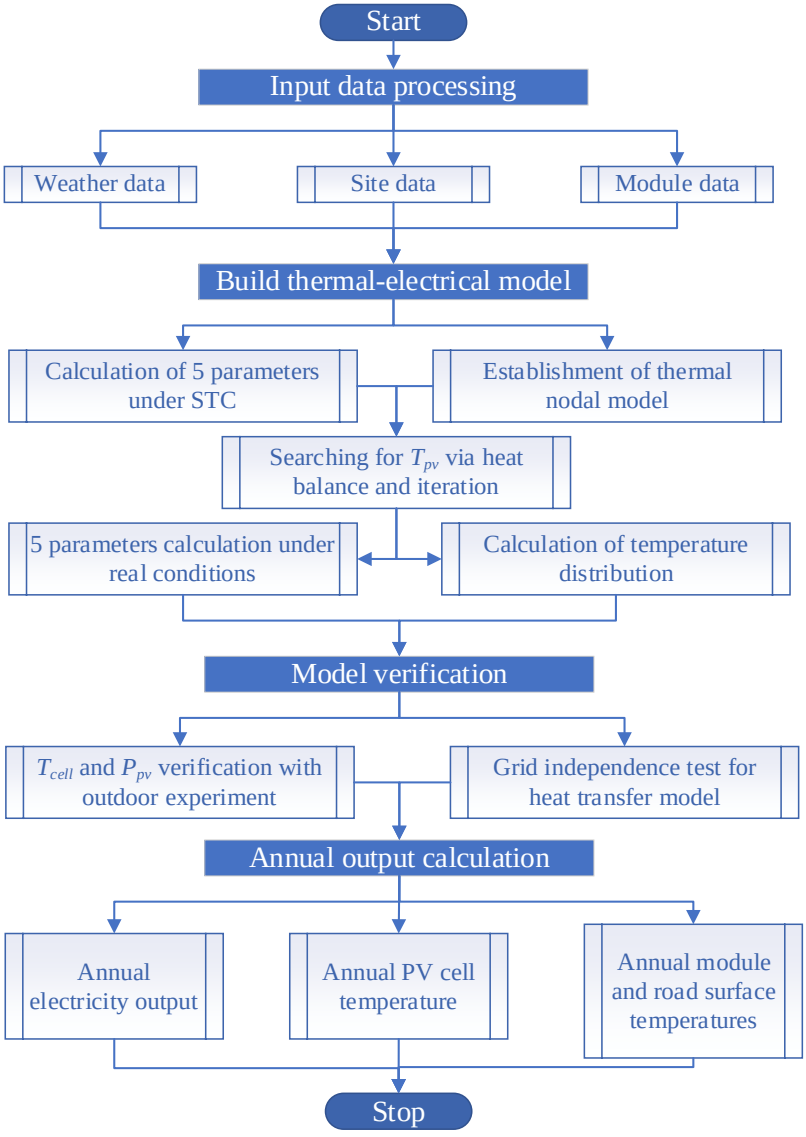

Fig. 3 Overview of this study

3.1 System mathematical modelling

The solar pavement module mathematical model is established from electrical and thermal aspects. This study uses the 5-parameter PV generation model of high accuracy for silicon-based PV road module. The 2-dimension heat transfer model with thermal nodes in the PV road module and surrounding ground zones is established to simulate the system temperature distribution. The

integration of the electrical model and thermal model is added to propose a novel thermal-electrical model, which is more suitable for PV road modules. Two statistical indicators, mean absolute error (MAE) and Root mean square error (RMSE), are commonly used for the model verification [46].

3.1.1 Electricity model

The single-diode 5-parameter model is utilized to simulate the PVP module output [47], with consideration of a series resistance and a parallel resistance, as shown in Fig. 4. The five parameters used in this study include diode thermal voltage V_t (V), series and parallel resistances R_{se} (Ω) and R_{pa} (Ω), photocurrent I_{pc} (A) and reserve saturation diode current I_0 (A). Based on the equivalent circuit model, the PV output I_{pv} (A) and V_{pv} (V) via the Shockley diode equation for one PV module could be presented as follows [48, 49]:

$$I_{pv} = I_{pc} - I_0 \left\{ e^{1/V_t \left(V_{pv}/N_{se} + I_{pv} \cdot R_{se} \right)} - 1 \right\} - \frac{1}{R_{pa}} \left(\frac{V_{pv}}{N_{se}} + R_{se} \cdot I_{pv} \right) \quad (1)$$

where N_{se} is the cell number in series.

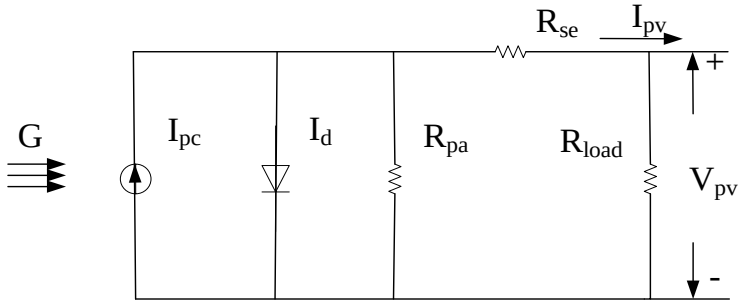

Fig. 4 Five-parameter electrical model

It could be seen that the equation for I_{pv} and V_{pv} calculation is inexplicit, which consumes a long calculation time. Thus, the equation could be expressed in the explicit form as follows:

$$I_{pv} = \left[-V_{pv} + N_{se} V_t \left(Lambert\ W \left(\frac{I_0 R_{se} R_{pa} \exp(A_1)}{N_{se} V_t (B_1)} \right) - A_1 \right) \right] / R_{se} \quad (2)$$

where $A_1 = \frac{R_{pa}(I_0 R_{se} + I_{pc} R_{se} + V_{pv})}{N_{se} V_t (R_{pa} + R_{se})}$, $B_1 = R_{pa} + R_{se}$, and the Lambert W function, $ye^y = x$, could be used for the analytical solution of the inexplicit equation for PV generation estimation [50].

The explicit equation for I_{pv} could be simplified as below:

$$I_{pv} = \frac{R_{se}(R_{pa}(I_0 + I_{pc}) - V_{pv}) - N_{se} V_t (B_1) \text{Lambert W} \left(\frac{I_0 R_{se} R_{pa} \exp(A_1)}{N_{se} V_t (B_1)} \right)}{R_{se} (B_1)} \quad (3)$$

The PV output is simulated under the non-standard test real condition based on the five reference parameters under standard test condition (STC) [51]. The five reference parameters under STC, V_{tSTC}, I_{pcSTC}, I_{0STC}, R_{paSTC} and R_{seSTC}, could be calculated as presented [52]:

$$\begin{cases} V_{tSTC} = \dfrac{K_v \cdot T_{cSTC} - V_{ocSTC}}{\dfrac{N_{se} \cdot T_{cSTC} \cdot K_i}{I_{pcSTC}} - 3N_{se} - \dfrac{E_g \cdot N_{se}}{k \cdot T_{STC}}} \\ I_{pcSTC} \approx I_{scSTC} \\ I_{0STC} = I_{scSTC} \cdot e^{-\frac{V_{ocSTC}}{N_{se} \cdot V_{tSTC}}} \\ R_{paSTC} = \dfrac{(V_{mSTC} - I_{mSTC} \cdot R_{seSTC}) \cdot (V_{mSTC} - N_{se} \cdot V_{tSTC})}{(V_{mSTC} - I_{mSTC} \cdot R_{seSTC}) \cdot (I_{scSTC} - I_{mSTC}) - N_{se} \cdot V_{tSTC} \cdot I_{mSTC}} \\ I_{mSTC} = I_{pcSTC} - I_{0STC} \left[e^{\frac{V_{mSTC} + I_{mSTC} \cdot R_{seSTC}}{N_{se} \cdot V_{tSTC}}} - 1 \right] \\ - \dfrac{(V_{mSTC} + I_{mSTC} \cdot R_{seSTC}) \cdot [(V_{mSTC} - I_{mSTC} \cdot R_{seSTC}) \cdot (I_{scSTC} - I_{mSTC}) - N_{se} \cdot V_{tSTC} \cdot I_{mSTC}]}{(V_{mSTC} - I_{mSTC} \cdot R_{seSTC}) \cdot (V_{mSTC} - N_{se} \cdot V_{tSTC})} \end{cases} \quad (4)$$

where K_v/K_i is the voltage/current temperature coefficient (%/°C), T_{cSTC} is the cell temperature under STC (°C), E_g is the band gap, set as 1.121 [48] for silicon cell (eV), I_{scSTC} is the short circuit current under STC (A), V_{ocSTC} is the open circuit voltage under STC (V), k is the Boltzmann's constant 1.381×10^{-23} (J/K), I_{mSTC} is the current at maximum power point under STC (A), V_{mSTC} is the voltage at maximum power point under STC (V).

The PV 5 parameters for practical conditions, I_{pc}, I_0, R_{se}, R_{pa} and V_t, could be simulated as shown [47]:

$$\begin{cases} I_{pc} = \dfrac{G_s}{G_{sSTC}} \cdot I_{pcSTC} \cdot [1 + K_i \cdot (T_c - T_{cSTC})] \\ I_0 = I_{0STC} \cdot \left(\dfrac{T_c}{T_{cSTC}}\right)^3 e^{\frac{qE_g}{k} \cdot \left(\frac{T_c - T_{cSTC}}{T_{cSTC} \cdot T_c}\right)} \\ R_{se} = R_{seSTC} \\ R_{pa} = \dfrac{G_{sSTC}}{G_s} \cdot R_{paSTC} \\ V_t = \dfrac{T_c}{T_{cSTC}} \cdot V_{tSTC} \end{cases} \quad (5)$$

where G_s is solar irradiance (W/m^2), G_{sSTC} is the solar irradiance under STC (W/m^2), T_c is the PV cell temperature (K), q is the electron charge, at 1.602×10^{-19} (C)

The PV efficiency η_{pv} stands for the electricity generation ratio of the total received solar radiation, as presented below:

$$\eta_{pv} = \frac{I_m \cdot V_m}{G_s \cdot A} \quad (6)$$

where I_m is the PV output current at maximum power point (A), V_m is the PV output voltage at maximum power point (V) and A is the surface area of the PV road module (m^2).

3.1.2 Partial shading influence on electrical output

Due to the application situation of road pavement of the PVP module, the shading from vehicle, tree, telegraph pole, etc. may influence the PVP power output. The shading ratio, x_{pv}, is the crucial parameter to simulate the module electrical performance, which could be calculated as follows:

$$x_{pv} = \frac{G_{sd}}{G_{sSTC}} \tag{7}$$

where G_{sd} is the received solar irradiance of the solar cell under the shading condition (W/m^2).

The slight shading at the very beginning reduces the power generation of the shaded solar cell, while it still works at the forward biased condition, decreasing the panel current due to the series connection of shaded and unshaded solar cells. If the shading condition is severe which make the shaded cell reversed and the cell does not reach the breakdown condition, the solar cell current could be simulated with the quadratic factor u_{pv} as below [53]:

$$I_{pv} = I_{ph} + u_{pv}\left(V_{pv} + I_{pv} \cdot R_{se}\right)^2 \tag{8}$$

To alleviate the burden from the partial shading solar cell, the bypass diodes [54] are connected to the solar cell string in parallel and will be conducted if the reversed string voltage is over the threshold voltage. In this study, the module only contains 9 solar cells or 18 half-solar cells so the effect of the bypass diodes are not obvious, but the influence of partial shading with bypass diodes will be considered in the future manufacturing with larger size and amount.

3.1.3 Heat transfer model

The heat transfer model is simulated based on thermal nodes, as shown in Fig. 5, and the assumptions of the two-dimension thermal nodal model of this study are presented as follows:

(a) The PV module ohmic losses and the ground evaporation latent heat are ignored;

(b) The ground/PVP module thermophysical properties are fix with temperature variations, and the ground is assumed homogeneous;

(c) The sky is considered a big blackbody.

The time step is selected fix at 30s to meet the convergence condition from the Fourier numbers of different thermal nodes and reduce the computation time for year-long simulation. Due to the adiabatic condition of the axle wire of the PVP module shown in Fig. 5, the total model is simulated by half. The spatial steps of the x and y axes are selected at 0.05m and 0.04m, respectively. The grid independence test can be found in Section 4.1.2. The spatial ranges are set as 3m for x-axis and 4m for y-axis.

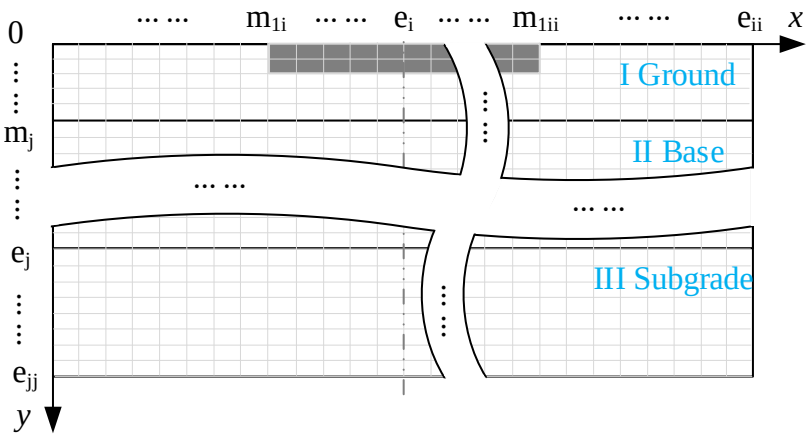

Fig. 5 Thermal nodal model diagram

The boundary conditions of the PV module/ground at t>0 are shown as follows:

$$k\frac{\partial T}{\partial y} = Q, 0 < x < e_i, y = 0 \tag{9}$$

$$\frac{\partial T}{\partial x} = 0, \ \ x = 0/e_i, 0 < y < e_{jj} \tag{10}$$

$$T_{gd} = T_{ini}, \ 0 \le x \le e_i, y = e_{jj} \tag{11}$$

where k is the thermal conductivity of ground or PV module (W/m/K), T is the temperature of ground or PV module (℃), Q is the heat flux of ground, PV surface or PV cell as shown in Eq. 11-13 and T_{ini} is the initial temperature (℃) of all the nodes at (t=0) and is determined by the local annual average ambient temperature [55].

In the finite difference method (FDM), the EFDM (explicit) and IFDM (implicit) are both included and used alternatively. Utilizing the EFDM relative to IFDM enables higher calculation efficiency and using IFDM relative to EFDM expands the applicability for larger time and spatial steps. Therefore, to improve the calculation efficiency without sacrificing prediction accuracy, the alternate direction FDM is utilized for solving the ground equations to get the temperature responses.

According to the model assumptions, it should be noted that the thermophysical properties of the ground and PV are both assumed to be constants. Thus, the conductive governing equations of ground in the cylindrical coordinate system could be obtained by Fourier's principle as follows:

$$\frac{1}{a_{gd}}\frac{\partial T_{gd,li}}{\partial t} = \frac{\partial^2 T_{gd,li}}{\partial x^2} + \frac{\partial^2 T_{gd,li}}{\partial y^2} \ or \ \frac{1}{a_{pv}}\frac{\partial T_{pv}}{\partial t} = \frac{\partial^2 T_{pv}}{\partial x^2} + \frac{\partial^2 T_{pv}}{\partial y^2} \tag{12}$$

where T_{gd} is the ground temperature (℃), a_{gd} and a_{pv} are the thermal diffusivity of ground and PV (m^2/s), equal to $\frac{k}{\rho c}$ for the different materials, t is the simulation time (s) and T_{pv} is the temperature (℃) of PV surface or PV cell.

The ground surface heat flux Q_{gd} (W/m^2) is presented as follows:

$$Q_{gd} = \alpha_{gd} G_s + \varepsilon_{gd}\sigma \begin{pmatrix} (T_{sky} + 273.15)^4 \\ -(T_{gd} + 273.15)^4 \end{pmatrix} + h(T_a - T_{gd}) \quad (13)$$

where α_{gd} and ε_{gd} are the absorptivity and emissivity of ground, σ is the Stefan-Boltzmann constant, at 5.67×10^{-8}W/m^2/K^4, h is the convective heat transfer coefficient (W/m^2/°C), equals $5.8+3.9v_{win}$ ($v_{win} \leq 5m/s$) or $7.1{v_{win}}^{0.78}$ ($v_{win} > 5m/s$) [56], T_{sky} is the equivalent sky temperature (°C), calculated by $T_{sky}=0.0552T_a^{1.5}$ in K unit [57], and T_a is the ambient air temperature (°C).

The PV surface heat flux Q_{pvs} (W/m^2) could be shown as:

$$\begin{aligned} Q_{pvs} = \alpha_g G_s + \varepsilon_g\sigma\left((T_{sky} + 273.15)^4 - (T_{pvs} + 273.15)^4\right) \\ +h(T_a - T_{pvs}) + \varepsilon_c\tau_g\sigma\left((T_{cell} + 273.15)^4 - (T_{pvs} + 273.15)^4\right) \end{aligned} \quad (14)$$

where α_g, ε_g and τ_g are the absorptivity, emissivity and transmissivity of the tempered glass, T_{pvs} and T_{cell} are the PV surface and cell temperatures (°C).

The heat flux of PV cell Q_{cell} (W/m^2) in thermal nodal is displayed as follows:

$$Q_{cell} = \alpha_c\tau_g G_s + \varepsilon_c\tau_g\sigma\left((T_{pvs} + 273.15)^4 - (T_{cell} + 273.15)^4\right) \quad (15)$$

The heat balance equations of the PV module and the ground zone are similar; thus, the temperature distribution of the ground is shown as the example for model explanation, which can be described as:

$$\begin{aligned} (\rho c)_{gd}\Delta x\Delta y \cdot \frac{T_{gd}^{p+1}(i,j) - T_{gd}^{p}(i,j)}{\Delta\tau} = \Delta y \cdot \frac{T_{gd}^{p}(i-1,j) - T_{gd}^{p}(i,j)}{\Delta x} \cdot k_{gd} \\ +\Delta y \cdot \frac{T_{gd}^{p}(i+1,j) - T_{gd}^{p}(i,j)}{\Delta x} \cdot k_{gd} + \Delta x \cdot \frac{T_{gd}^{p}(i,j-1) - T_{gd}^{p}(i,j)}{\Delta y} \cdot k_{gd} \\ +\Delta x \cdot \frac{T_{gd}^{p}(i,j+1) - T_{gd}^{p}(i,j)}{\Delta y} \cdot k_{gd} + Q_{gd} \cdot \Delta x \end{aligned} \quad (16)$$

$$\begin{aligned} (\rho c)_{gd}\Delta x\Delta y \cdot \frac{T_{gd}^{p+1}(i,j) - T_{gd}^{p}(i,j)}{\Delta\tau} = \Delta y \cdot \frac{T_{gd}^{p+1}(i-1,j) - T_{gd}^{p+1}(i,j)}{\Delta x} \cdot k_{gd} \\ +\Delta y \cdot \frac{T_{gd}^{p+1}(i+1,j) - T_{gd}^{p+1}(i,j)}{\Delta x} \cdot k_{gd} + \Delta x \cdot \frac{T_{gd}^{p+1}(i,j-1) - T_{gd}^{p+1}(i,j)}{\Delta y} \cdot k_{gd} \\ +\Delta x \cdot \frac{T_{gd}^{p+1}(i,j+1) - T_{gd}^{p+1}(i,j)}{\Delta y} \cdot k_{gd} + Q_{gd} \cdot \Delta x \end{aligned} \quad (17)$$

where p is the numerical time series, equals $\frac{t}{\Delta t}$, $(\rho c)_{gd}$ is the product of ground density (kg/m^3) and specific heat capacity (J/kg/K), k_{gd} is the heat conductivity (W/m/K) of the ground material.

The above equations for different layers li, (l_1 l_2 l_3) could be simplified as presented:

$$T_{gd}^{p+1}(i,j) = \left(1 - N_{2,li}\right)T_{gd}^{p}(i,j) + 0.5N_{2,li}T_{gd}^{p}(i,j+1) + 0.5N_{2,li}T_{gd}^{p}(i,j-1) + \left(1 - N_{1,li}\right)T_{gd}^{p}(i,j) + 0.5N_{1,li}T_{gd}^{p}(i+1,j) + 0.5N_{1,li}T_{gd}^{p}(i-1,j) \quad (18)$$

$$T_{gd}^{p}(i,j) = \left(1 + N_{1,li}\right)T_{gd}^{p+1}(i,j) - 0.5N_{1,li}T_{gd}^{p+1}(i+1,j) - 0.5N_{1,li}T_{gd}^{p+1}(i-1,j) + \left(1 + N_{2,li}\right)T_{gd}^{p+1}(i,j) + 0.5N_{1,li}T_{gd}^{p}(i+1,j) + 0.5N_{1,li}T_{gd}^{p}(i-1,j) \quad (19)$$

where $N_1 = \frac{2a\Delta t}{(\Delta x)^2}$, $N_2 = \frac{2a\Delta t}{(\Delta y)^2}$, $N_{h1} = \frac{2a\Delta t}{k\Delta y}$, $a = \frac{\lambda}{\rho c}$.

The nodal equations at (0,0) via alternative direction difference method (ADDM) are presented below:

$$\left(1 + N_{1,l1}\right)T_{gd}^{p+1}(0,0) - N_{1,l1}T_{gd}^{p+1}(1,0) = \left(1 - N_{2,l1}\right)T_{gd}^{p}(0,0) + N_{2,l1}T_{gd}^{p}(0,1) + N_h Q_{gd} \quad (20)$$

$$\left(1 + N_{2,l1}\right)T_{gd}^{p+1}(0,0) - N_{2,l1}T_{gd}^{p+1}(0,1) = \left(1 - N_{2,l1}\right)T_{gd}^{p}(0,0) + N_{2,l1}T_{gd}^{p}(1,0) + N_h Q_{gd} \quad (21)$$

The specific nodal equations could be found in the Appendix for a more concise explanation. To show the difference of electrical and thermal-electrical model, the equations related to PV cell are shown.

The energy balance of PV module surface (m_i<x<e_i, 0) can be displayed as:

$$\left(1 + N_{1,pv}\right)T_{pvs}^{p+1}(i,) - 0.5N_{1,pv}T_{pvs}^{p+1}(i+1,0) - 0.5N_{1,pv}T_{pvs}^{p+1}(i-1,0) = \left(1 - N_{2,pv}\right)T_{pvs}^{p}(i,0) + N_{2,pv}T_{cell}^{p}(i,1) + N_h Q_{pvs} \quad (22)$$

$$\left(1 + N_{2,pv}\right)T_{pvs}^{p+1}(i,0) - N_{2,pv}T_{cell}^{p}(i,1) - N_h Q_{pvs} = \left(1 - N_{1,pv}\right)T_{pvs}^{p}(i,0) + 0.5N_{1,pv}T_{pvs}^{p}(i+1,0) + 0.5N_{1,pv}T_{pvs}^{p}(i-1,0) \quad (23)$$

The equations for the PV cell layer (m_i<x<e_i, 1) are expressed below:

$$\left(1 + N_{1,pv}\right)T_{cell}^{p+1}(i,1) - 0.5N_{1,pv}T_{cell}^{p+1}(i+1,1) - 0.5N_{1,pv}T_{cell}^{p+1}(i-1,1) = \left(1 - N_{2,pv}\right)T_{cell}^{p}(i,1) + 0.5N_{2,pv}T_{cell}^{p}(i,0) + 0.5N_{2,pv-l1}T_{gd}^{p}\left(i,m_{1j}\right) + N_h Q_{cell} \quad (24)$$

$$\left(1 + N_{2,pv}\right)T_{cell}^{p+1}(i,1) - 0.5N_{2pv}T_{cell}^{p}(i,0) - 0.5N_{2,pv-l1}T_{gd}^{p}\left(i,m_{1j}\right) - N_h Q_{cell} = \left(1 - N_{1,pv}\right)T_{cell}^{p}(i,0) + 0.5N_{1,pv}T_{cell}^{p}(i+1,0) + 0.5N_{1,pv}T_{cell}^{p}(i-1,0) \quad (25)$$

The boundary of PV module surface (e_i, 0) is displayed as follows:

$$\left(1 + N_{1,pv}\right)T_{pvs}^{p+1}(e_i,0) - N_{1,pv}T_{pvs}^{p+1}(e_i - 1,0) = \left(1 - N_{2,pv}\right)T_{pvs}^{p}(e_i,0) + N_{2,pv}T_{pvs}^{p}(e_i,1) + N_h Q_{pvs} \quad (26)$$

$$\left(1+N_{2,pv}\right)T_{pvs}^{p+1}(e_i,0)-N_{2,pv}T_{pvs}^{p+1}(e_i,1)=$$
$$\left(1-N_{1,pv}\right)T_{pvs}^{p}(e_i,0)+N_{1,pv}T_{pvs}^{p}(e_i+1,0)-N_hQ_{pvs} \quad (27)$$

Likewise, the boundary of the PV cell layer (e_i, 1) could be expressed in the following equations:

$$\left(1+N_{1,pv}\right)T_{cell}^{p+1}(e_i,1)-N_{1,pv}T_{pvs}^{p+1}(e_i-1,0)=$$
$$\left(1-N_{2,pv}\right)T_{cell}^{p}(e_i,1)+0.5N_{2,pv}T_{pvs}^{p}(e_i,0)$$
$$+0.5N_{2,pv-l1}T_{gd}^{p}\left(e_i,m_{1j}\right)+N_hQ_{cell} \quad (28)$$

$$\left(1+N_{2,pv}\right)T_{cell}^{p+1}(e_i,1)-0.5N_{2,pv}T_{pvs}^{p+1}(e_i,0)-0.5N_{2,pv-l1}T_{gd}^{p+1}\left(e_i,m_{1j}\right)=$$
$$\left(1-N_{1,pv}\right)T_{cell}^{p}(e_i,1)+N_{1,pv}T_{cell}^{p}(e_i+1,1)-N_hQ_{cell} \quad (29)$$

3.1.4 Thermal-electrical model

The thermal and electrical models of the PV road modules are combined together through the energy balance of the PV cell layer, namely the PV cell temperature. The differences between the two models lie in the heat flux of PV cells in the thermal-electrical is displayed:

$$Q_{cell}=\alpha_c\tau_gG_s+\varepsilon_c\tau_g\sigma\begin{pmatrix}\left(T_{pvs}+273.15\right)^4\\-(T_{cell}+273.15)^4\end{pmatrix}-P_{pv}/A \quad (30)$$

3.2 Grid independence test

For the numerical heat transfer model utilizing the ADDM, the necessary grid independence test to avoid the interference caused by radial and bottom BCs has been conducted, and the result is shown in Fig. 6 for the node temperatures at the PV cell layer center at 8748 and 8760 hours in the year-long simulation. The grid number for this study is 6000, which is larger than 4500, the turning point in the figure; thus, the thermal nodal result is reliable and not influenced by the grid number.

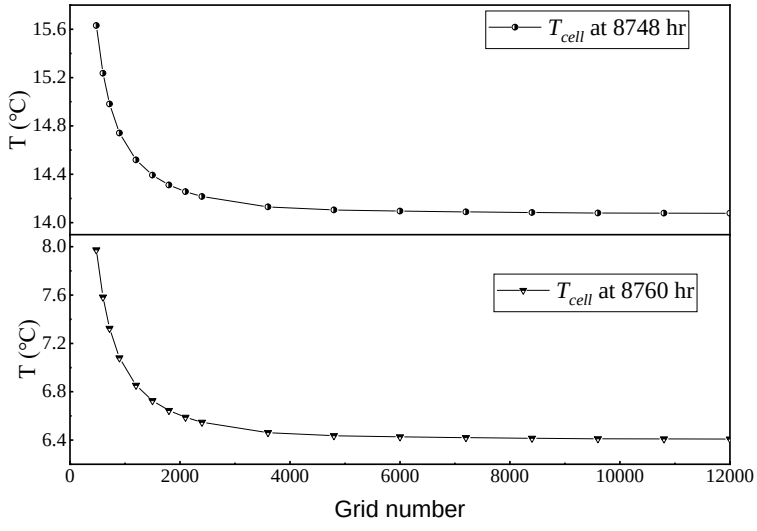

Fig. 6 Grid independence test for thermal nodal model

3.3 Module component specification

The specifications of the components are shown in this section. The basic information on the prefabricated PV module is displayed in Table 1, which includes significant parameters in the electrical model from the manufacturer and the previous study in our group. The crucial material thermal properties for different layers in the thermal model have been shown in Table 2. For each kind of thermal nodes, the thermal properties of the interface are the equivalent ones via weighted mean according to the volume of the material. The practical considerations of PV output are considered, including the MPPT efficiency (99.5%) [58], the PV attenuation presented in Table 1, and other factors like wire loss and dusting (80%) [59].

Table 1 PV module parameter

Parameter	Value	Parameter	Value
Efficiency (%)	20	Type	Mono-Si
Cell number	9	Surface transparency (%)	90
P_{max} (W)	31.5	Volume (mm×mm×mm)	500×500×40
V_{oc} (V)	5.4/10.8	Series	9
I_{sc} (A)	7.5/3.75	Parallel	1
V_{mp} (V)	4.5/9.0	m (kg)	13
I_{mp} (A)	7.0/3.5	Guaranteed attenuation η_{df} (%, yr)	5%, 5; 10%, 12; 20%, 25
K_i (A/ (%℃))	0.057	Frame material	Al-alloy
K_v (V/ (%℃))	-0.286	Work temperature (℃)	-40~85
K_p (W/ (%℃))	-0.370	Load capacity (kPa) [60]	74

Table 2 Specifications of the materials in the simulation model.

Material	Absorptivity	Emissivity	Density	Specific heat capacity	Thermal conductivity
Unit	-	-	kg/m^3	J/kg/K	W/m/K
Tempered glass [32]	0.02	0.9	2200	670	1.1
Asphalt concrete [33, 35]	0.95	0.91	2238	920	1.8
Concrete	0.75	0.90	1800	840	1.3
EVA [14]	-	-	2090	960	0.35
PV cell [32, 33, 61]	0.90	0.88	2330	900	140
Subgrade [14]	-	-	1920	900	1.3
Base [14]	-	-	2200	900	1.8
Air	-	-	1.2	1005	0.0263
EP [62]	-	-	1050	550	2.2

4 Experimental study

4.1 Lab test for PV module

The PVP module is first tested in the solar simulator lab via the solar simulator and IV-tracker with a pyranometer. The detail of the test rig could be found in the previous study of the research group [60]. The module figure and systematic diagram for the PV module lab test can be seen in Fig. 7. The front and rear side temperatures of the PV panel in the module are measured via T-type and Pt100 temperature sensors. The solar irradiance is adjusted through the test rig height variation and

switching on and off for the simulator lamps. The data are collected by the IV-tracker, data logger, and PC near the experimental rig.

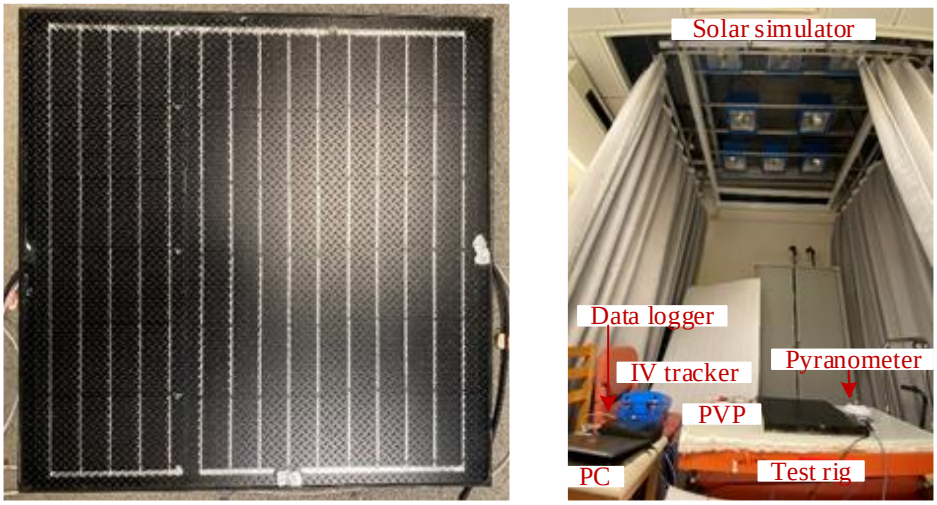

(a) (b)

Fig. 7 PV module lab test: (a) PVP module; (b) Module on the test rig.

The outdoor test of the PV road module is conducted on the campus of the Hong Kong Polytechnic University for two consecutive days in September when the solar irradiance is sufficient. The latitude and longitude of the site are selected at 22°18'N and longitude 114°10'E, with site altitude at 40m. The specific site is selected to have no shading during the entire daytime. The outdoor test system is displayed in Fig. 8. The global horizontal solar irradiance is collected by the pyranometer shown in Fig. 8 (b) with the IV tracker for the PV panel measuring the I-V curve at 1 min intervals in Fig. 8 (c). The module surface temperature is tested via three T-type temperature sensors shown in Fig. 8 (d). The PV cell rear side temperature is collected through the four Pt 100 temperature sensors, which can be found in Fig. 8 (e). As presented in Fig. 8 (f), the meteorological station is utilized to measure the primary weather conditions with relative humidity, ambient temperature, and wind velocity.

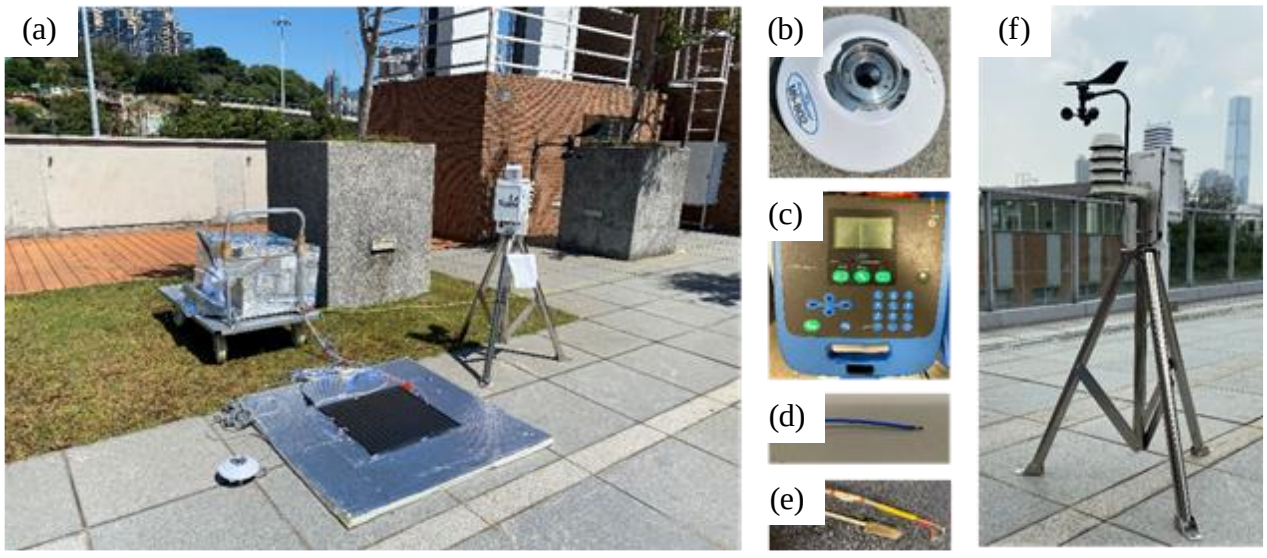

Fig. 8 Outdoor test for PV module: (a) test system; (b) pyranometer; (c) I-V tracker; (d) T-type temperature sensor; (e) Pt 100 temperature sensor; (f) meteorological station.

4.2 Surface anti-skid property test and free-falling ball impact test

The anti-slipping surface feature is crucial to the road module, and the surface frictional property is tested by the British pendulum tester, according to Standard ASTM E770-80 [63]. The four sides of the PV road module at dry and wet conditions are tested at 25℃, as shown in Fig. 9.

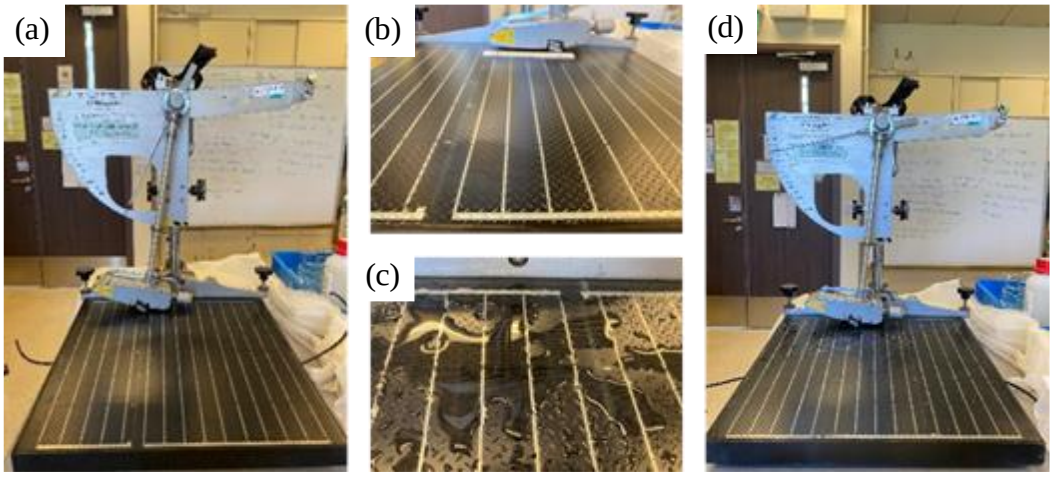

Fig. 9 Friction test:(a) Tester with dry road module; (b) day road surface; (c) wet road surface; (d) tester with wet road module.

4.3 Equipment specifications

The major equipment specifications are displayed in Table 3. The solar measurement equipment from EKO is utilized for the electrical test, Pt100 and K-type sensors are used for the heat temperature collection, and the standard British pendulum tester is used for the structural experiments.

Table 3 Equipment specifications

Item	Specification	Item	Specification
Solar simulator	Honle uv technology SOL1200	Pt100 testing range	0-100℃
Pyranometer	EKO MS-802 (A level)	Pt100 sensitivity	±0.1℃
Pyranometer sensitivity	7.13μV/(W/m^2)	T-type sensor sensitivity	±0. 5℃
Data logger	GRAPHTEC GL840	EKO IV tracker	MP11

5 Results and discussion

The experimental and simulation results of this study are presented in this Section. The PV generation under different partial shading conditions and solar irradiances are studied during lab tests. Grid independent test result for the thermal nodal model via the FDM method is shown in Section 3.2. The sunny day daily outdoor test has been conducted for PV road module crucial electrical and thermal performance and is utilized for proposed model verification. The other experiment results on structural and anti-skidding features have also been discussed. Regarding the simulation results, the parametric analyses have been conducted on crucial parameters, backfilling materials and surrounding ground materials, providing references for further design of PV road modules. The annual technical and thermal performances of PV road modules in two specific cases, Hong Kong

and Shanghai, have been analyzed and discussed in detail. The module thermal performance and electricity generation potential have been compared nationwide in China.

5.1 Experimental results

5.1.1 PV lab test on partial shading

As shown in Fig. 10, the PVP module output curves (current-voltage and power-voltage) are measured during lab test with different partial shading conditions (x_{pv} for three PV cells increases from 0 to 5/6 at the interval of 1/6). If the entire solar cell is shaded, the cell will not generate the electricity, thus the current in the series is reduced to 0. Two different solar irradiance, 1000 and 500 W/m^2, are considered as the high and medium solar irradiance conditions. For the PVP module with 9 solar cells connected in one series, the partial shading on the solar cells mainly influences the PV output current and the power decreases mainly depends on the received solar irradiance. The maximum PV output decreases by 12.1%/12.2%, 33.9%/22.6%, 51.6%/49.9%, 74.6%/74.9%, and 94.9%/95.2% with the shaded 1/6, 2/6, 3/6, 4/6 and 5/6 areas for solar cells under high/medium solar irradiance, respectively.

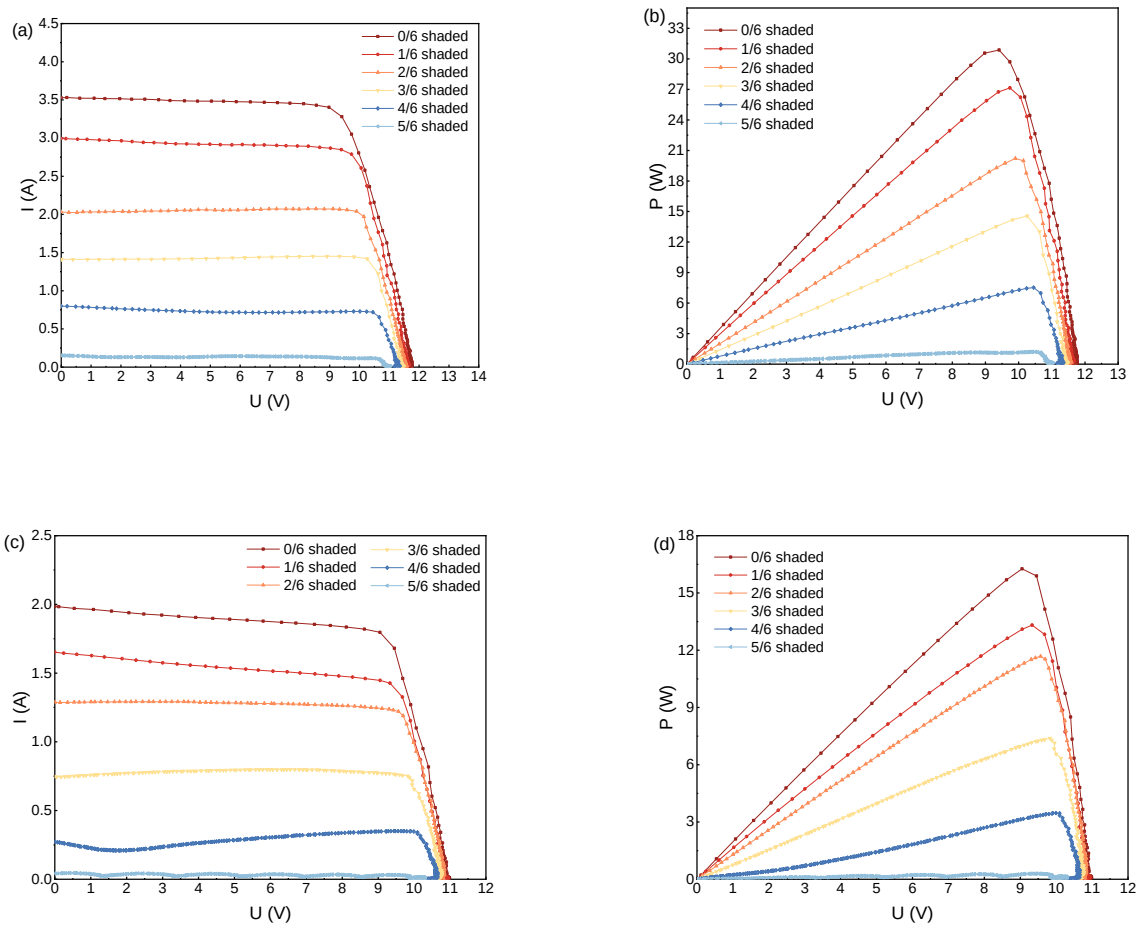

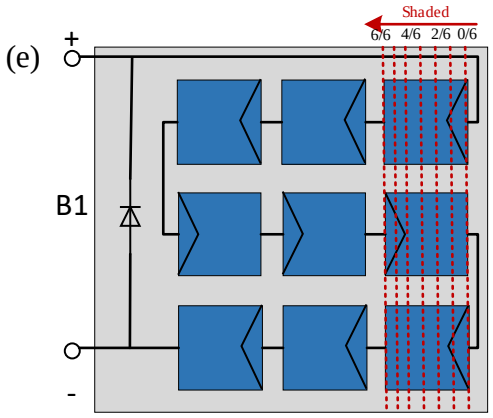

Fig. 10 PV output with different partial shading conditions under high and medium solar irradiance: (a) IV curve for 1000W/m^2; (b) PV curve for 1000W/m^2; (c) IV curve for 500W/m^2; (d) PV curve for 500W/m^2; (e) Different partial shading conditions.

5.1.2 Outdoor performance on a sunny day

The outdoor performance of the PV road module is conducted in Hong Kong, from 8.22 am to 5.00 pm Sep. 25th (sunny) in 2022. The weather data have been shown in Fig. 11. The ambient temperature T_{amb}, solar irradiance I_t, relative humidity (RH), and wind velocity V_{win} are shown with a time resolution of 1 min. The wind velocity is tested at around 1.5m from the ground, which may seem low for a meteorological station; however, the data is useful for a PV pavement module installed on the ground with high buildings around the site. The solar irradiance is sufficient, with accumulative Gs reaching 5.7 kWh/m^2, and maximum G_s at 933.6 W/m^2. The average T_{amb} for the sunny day is 31.7℃, while the maximum T_{amb} reaches 33.6 ℃.

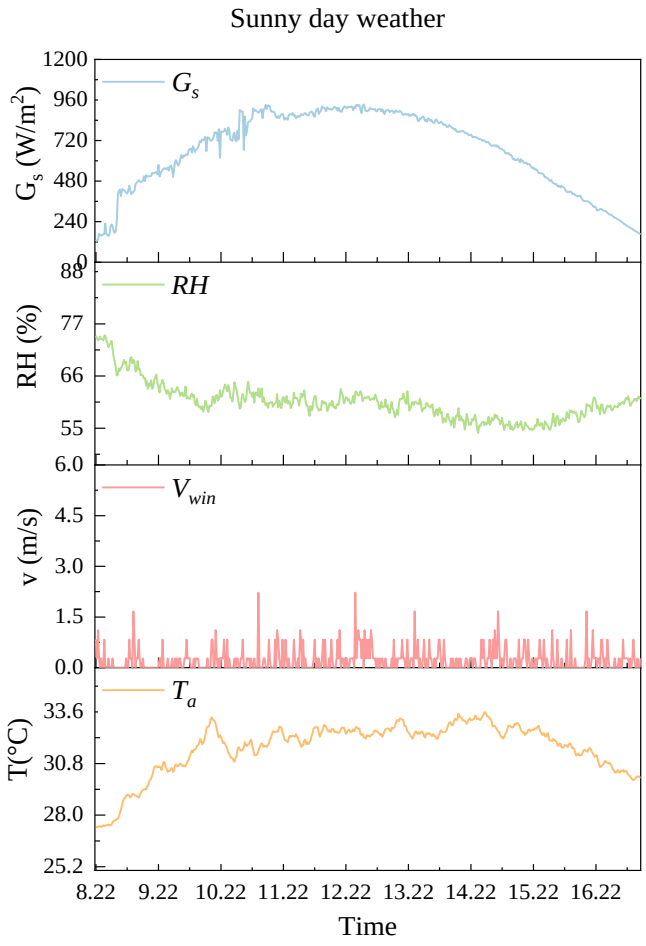

Fig. 11 Weather data of the sunny day

The PV-road module technical performances are presented in Fig. 12, with PV module surface and cell temperatures, T_{sur} and T_{cell}, PV output, P_{pv}, in light blue, orange, and red lines, and PV cell efficiency, η_{pv}, in light purple bar. The daily PV output of the sunny day is low, at 0.171 kWh (namely 0.684 kWh/m^2), for the relatively small PV cell area of approximately 0.008m^2 per 4 PV modules. The maximum PV output reaches 27.98 W for 1 PVP module. The temperatures of the surface and rear side of the PV panel of the module are measured, and the maximum gaps of maximum and average T_{cell} reach 3.86 ℃. The maximum PV generation efficiency reaches 14.71% on the sunny day, which is relatively low due to the low solar irradiance transmittance of the anti-skid layer with patterns and small PV cell area, with effective PV cell area at 0.002m^2. It should be mentioned that the experimental backfilling module is an air gap, which leads to a high PV cell temperature of over 70 ℃, as shown in work by Zhou et al. [37].

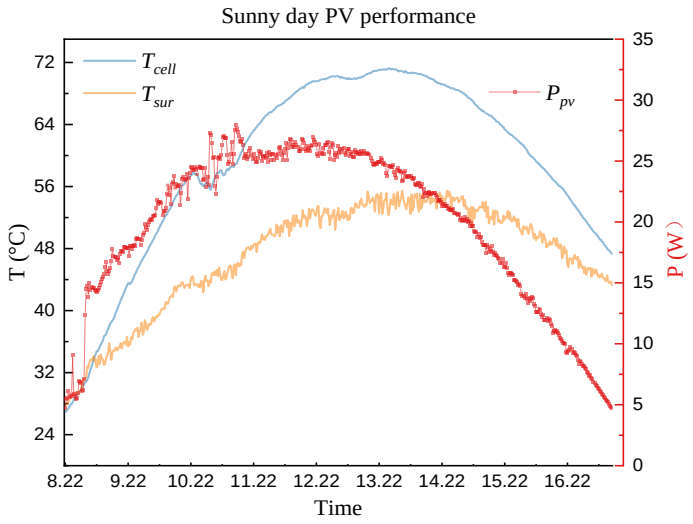

Fig. 12 PV module outdoor performance of the sunny day

5.1.3 Model verification

The proposed thermal-electrical model is verified based on the outdoor test on the sunny day. The conventional 5-parameter PV generation model with NOCT equation for PV cell temperature calculation is used as the comparison model for the electrical model. Also, the thermal nodal model, without considering the influence of PV electrical generation on PV cell temperature, is applied as the thermal performance comparison for the proposed PV road module mathematical model.

To supplement the basic electrical model and conventional thermal-electrical equation, the nominal operating cell temperature (NOCT) model, which is mainly utilized equation for PV cell calculation based on the weather data variation, could be shown as follows [58]:

$$T_{cell} = T_a + \frac{G_s}{G_{sSTC}} \cdot (NOCT) - 20 \tag{31}$$

The proposed thermal-electrical model verification of PV cell temperature and PV module generation output is shown in Fig. 13, and the corresponding statistics indicators are summarized in Table 4. Based on the PV cell temperature T_{cell} comparison of the thermal nodal model, NOCT model, and thermal-electrical model presented in Fig. 13 (a), the NOCT model is not applicable to the PV road circumstance with MAE and RMSE higher than 20% for the ground influence with ground heat conduction is not neglected instead of the unobvious heat convection of ambient air. The integration of the thermal nodal model and PV 5-parameter model increases the model accuracy or thermal performance, as the gap between orange and light green curves. However, the T_{cell} decrease of the proposed model from the thermal nodal model is not noticeable, only approximately 2% difference in MAE and RMSE, for the relatively low PV efficiency under high T_{cell} and high accuracy of the thermal nodal model with consideration of ground heat transfer. Regarding the PV electrical generation, as displayed in Fig. 13 (b), the proposed model performs better than the NOCT model integrated with the conventional PV electrical model with MAE and RMSE for P_{pv} reduced by 3.96% and 3.10%, respectively. The PV generation difference of the proposed model from the conventional electrical model is not so obvious due to the relatively low influence of cell temperature on the

module's electrical performance. However, the increase in accuracy of the proposed thermal-electrical model is explicit compared to the relatively low RMSE on P_{pv} of the conventional electrical model with approximately 33.41% improvement.

Table 4 Statistics indicators for different models

Indicators	Electrical model with NOCT	Thermal nodal model	Thermal-electrical model
T_{cell} MAE	-21.60%	3.83%	1.68%
T_{cell} RMSE	22.09%	5.20%	3.83%
P_{pv} MAE	7.56%	-	3.60%
P_{pv} RMSE	9.28%	-	6.18%

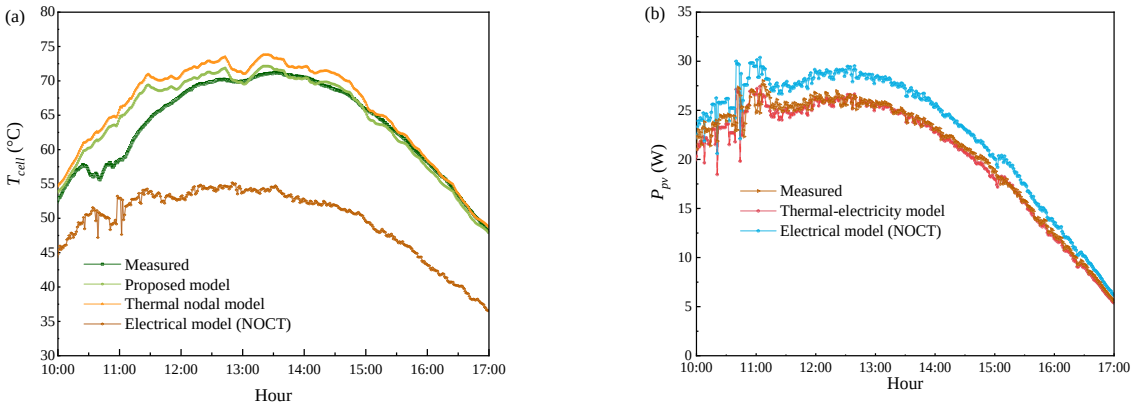

Fig. 13 Model verification of sunny day test: (a) thermal performance; (b) electrical generation.

5.1.4 Discussion on anti-skid road surface property

The standard test method for measuring surface frictional properties via the British Pendulum Tester with British Pendulum Number (BPN) is utilized in this study according to Standard ASTM E770-80 [63]. The experiment is repeated five times, and the mean result is used for both wet and dry conditions, as shown in Table 5. According to the transportation research laboratory in New Zealand, the mean result of the PVP module under wet condition is suitable for most primary road types [64]. Also, the result under the dry condition outperforms the previous study [21] with the anti-skid pattern on the PVP module surface.

Table 5 Results for surface frictional property test (ambient temperature 25℃, unit: BPN)

Condition	BPN 1	BPN 2	BPN 3	BPN 4	BPN 5	BPN mean	BPN mean	BPN mean
PVP module in study							PV panel [21]	PVP module in [21]
Dry								
Side 1	101	105	105	106	106	104.6		
Side 2	94	93	92	93	92	92.8	61.6	70
Side 3	112	112	112	114	114	112.8		
Side 4	115	115	115	114	114	114.6		
Wet								
Side 1	52	47	49	49	47	48.8	42	47.8

5.2 Simulated electrical and thermal performances of PVP module

5.2.1 Parametric analyses on backfilling and surrounding ground materials

The parametric analyses of the solar pavement module are conducted in this section. The PVP module backfilling material and surrounding ground material is varied in the year-long simulation for Hong Kong. Four consecutive days in typical summer (Aug.) and winter (Feb.) months were selected to show the technical performance variation of T_{cell}, T_{sur}, T_{road}, and P_{pv}. The different cases for parametric analyses are shown in Table 6. The filling material between the module frame and PV panel rear tempered glass varies from air to epoxy resin (EP). Also, two commonly used ground surrounding materials, cement and asphalt concrete are considered, with asphalt concrete selected for most of the cases, for it is the most suitable choice for urban roads.

Table 6 Cases for parametric analyses

Cases	Backfilling	Surrounding	Ground width (mm)
Base 1	-	Asphalt concrete	120
Base 2	-	Cement	120
Base S1	-	Asphalt concrete	40
Base S2	-	Asphalt concrete	200
Case 1	Air	Asphalt concrete	120
Case I	EP	Asphalt concrete	120
Case II	EP	Cement	120

(1) Surrounding ground variation

The T_{cell}, T_{road}, and T_{sur} with the surrounding ground variation of the PV road module are presented in Fig. 14 for HK and SH. The cement ground has lower heat conductivity, specific heat capacity, and density than the asphalt concrete road which has better heat transfer with the ground, while the asphalt concrete roadway has higher solar irradiance absorptivity which accepts more heat through solar irradiance. Thus, cement T_{road} (Base 2) has an apparent valley at night compared to asphalt concrete T_{road} (Base 1), which is higher than cement T_{road} due to the high diurnal inlet heat. Also, the temperature gap of two surrounding ground variations is more explicit in summer, especially for HK. The apparent heat island mitigation effect could be found in summer hours, as presented in Fig. 18 (b) and (d), and the maximum temperature gap of T_{road} and T_{sur} could reach 11.28℃ (HK) and 10.45℃ (SH) for asphalt concrete, and 9.46℃ (HK) and 8.27℃ (SH) for cement. Likewise, the maximum heat island alleviation via PVP module compared to the asphalt roadway and soil roadway could reach 9.4℃ [14] and 13.4℃ [7], respectively in typical summer days. The mean temperature gap during the previous experiments reaches approximately 4℃ for asphalt concrete roadway comparison.

Correspondingly, the PVP module on winter days could increase the road surface temperature, at 7.17℃ (HK) and 5.57℃ (SH) for asphalt concrete, 6.23℃ (HK) and 4.22℃ (SH) for cement in the selected days. The simulated temperature increase could help raise driving safety and provide some functions like road snow melting. The snow cover could be a barrier for PV generation and may influence the snow melting potential of the PVP module, however, the better heat conduction of the PVP module with the ground could also accelerate the snow melting speed [65]. After most of the

snow melt, the PV generation brings about more heat from the PV generation and maintains relatively high temperature compared to the conventional roadways.

When it comes to the T_{cell}, the asphalt concrete roadway brings about a tiny temperature increase compared to that of the cement roadway. However, the distinction between the two ground materials is not apparent within 1℃.

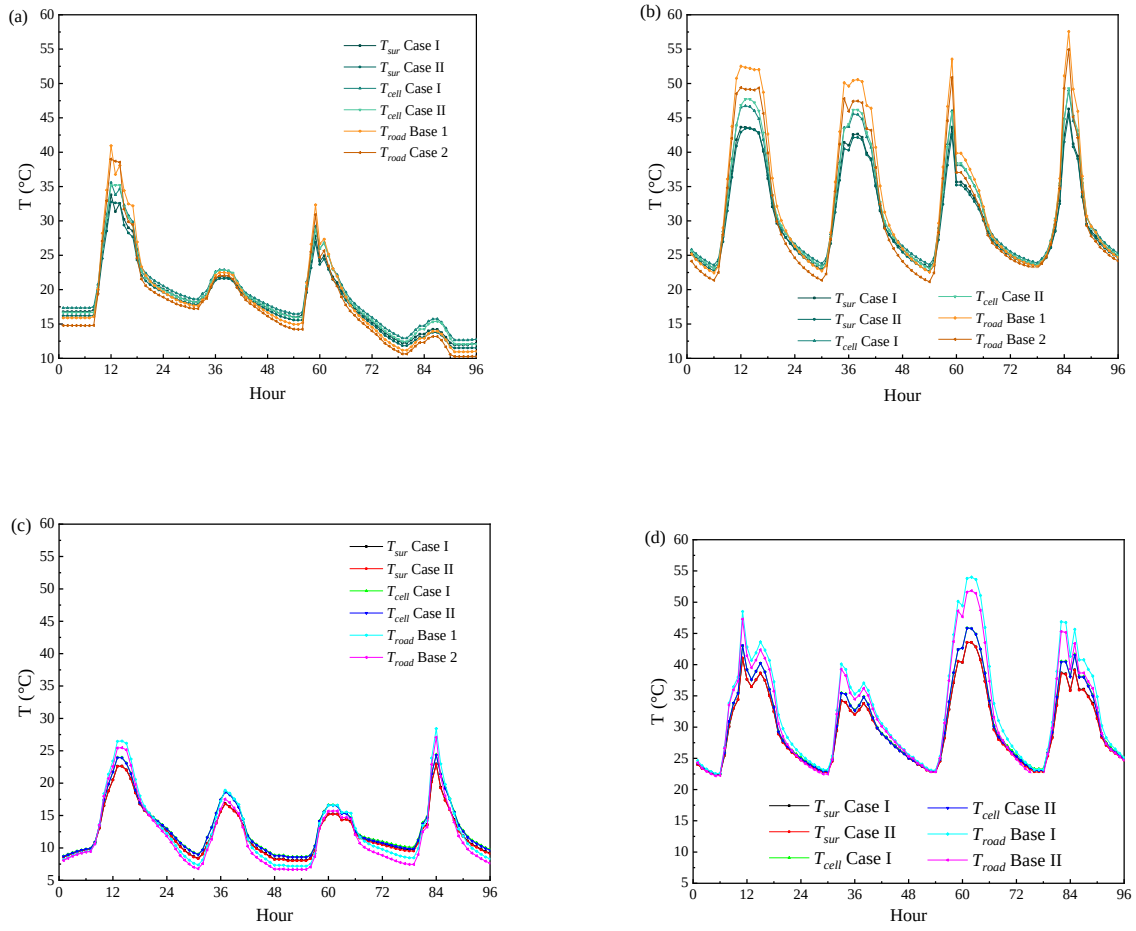

Fig. 14 T_{cell}, T_{road} and T_{sur} with surrounding ground material change: (a) HK in Feb.; (b) HK in Aug.; (c) SH in Feb.; (d) SH in Aug.

(2) Backfilling material change

The T_{cell}, T_{road}, and T_{sur} on the backfilling materials, air or EP, of the PV road module are presented in Fig. 15 for HK and SH. The surrounding ground material is selected as asphalt concrete as the significant reference in the studies of this field [45]. The EP filling is recommended compared to air gap for asphalt concrete roadways in HK and SH for the obvious lower T_{sur} and T_{cell}. The influence of the backfilling material is more obvious on HK summer days with higher ambient temperatures than on SH, with the T_{sur} and T_{cell} gaps reaching 4.32℃ and 11.68℃. Although the T_{sur} increase may have a positive effect to the roadway on winter days, reaching 3.59℃ and 2.55℃ for HK and SH, respectively, the heat island alleviation is reduced, which is more crucial to cities in southern China.

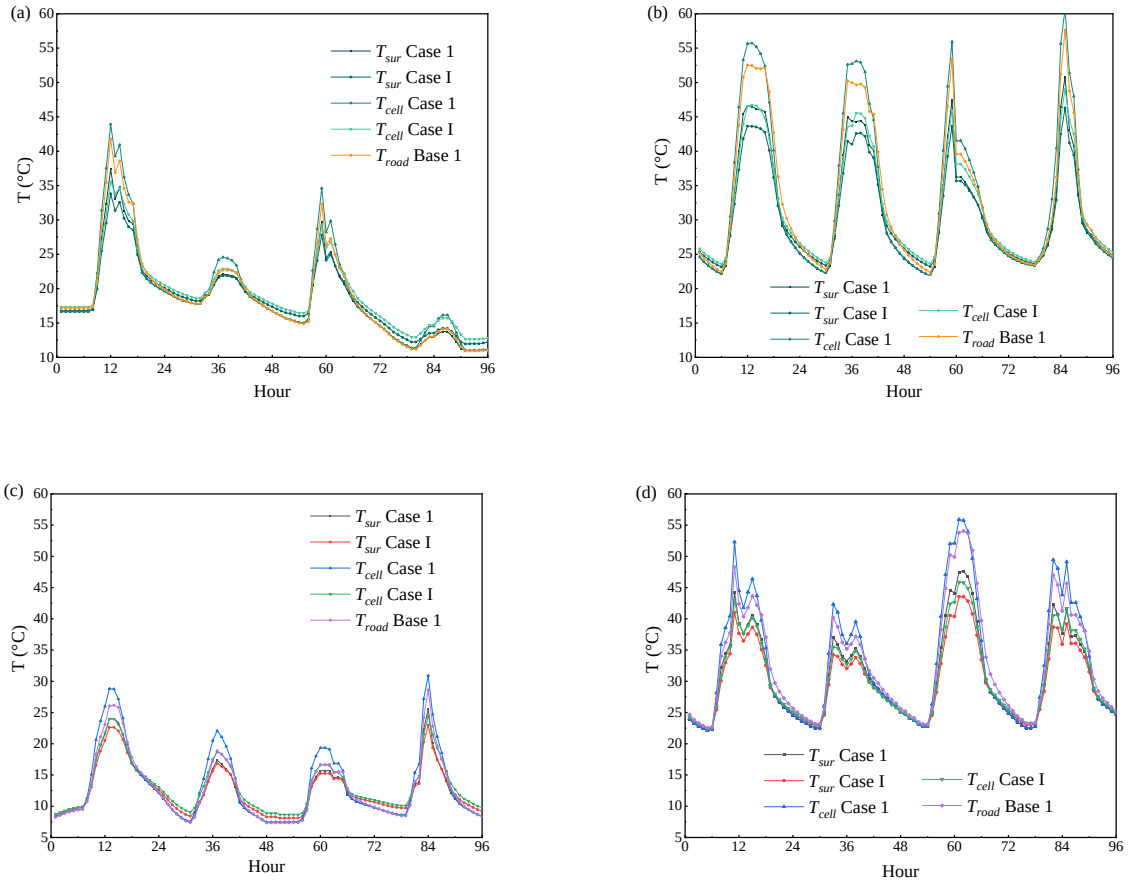

Fig. 15 T_{cell}, T_{road} and T_{sur} with filling ground material change: (a) HK in Feb.; (b) HK in Aug; (c) SH in Feb.; (d) SH in Aug.

5.2.2 Annual technical performances of PV road module in two cases

The crucial annual performance of PV generation, PV cell temperature, and module surface temperature, and the asphalt concrete road surface temperature, is displayed in Table 7. For better display, the PV output of the module has been transferred to the annual output (kWh) per Wp PV installation. The annual total and maximum PV output of Hong Kong (HK) with air filling outperform those of Shanghai (SH) by 6.44% and 2.87%, respectively, due to the significant solar irradiance difference. The backfilling material variation from air to EP increases the heat conductivity. The annual total E_{pv} increase could be further increased to 1.012 kWh/Wp from 1.010 kWh/Wp for SH with lower solar irradiance to HK by 0.3%.

Although the PV output increase is not apparent due to the 0.1% scale for the temperature coefficients shown in Table 1, the temperature variations under different conditions are explicit. Thus the heat island effect alleviation could be achieved with air and EP fillings. The urban heat island effect reduction (average T_{road} and T_{sur} gap) via EP filling is less effective in SH by 1.09℃, compared to HK at 1.14 ℃. Besides, it could also be found that the maximum T_{road} could be reduced and the minimum T_{road} could be increased by the substitution of conventional asphalt concrete pavement with PV pavement. The heat island effect alleviation of EP filling module is more noticeable than that of air filling in the city with a higher annual average T_{road} by 13.16℃, compared with SH by 11.38℃. However, when it comes to heat insulation in winter, the surface in the city with lower T_{road} could

have a more prominent effect on road snow melting, which could increase the minimum T_{road} from -1.10℃ to a minimum T_{road} above 0℃ via module with EP filling. Moreover, it could also be found that the maximum T_{cell} could be decreased to 47.53℃ and 53.29℃ for SH and HK, which outperforms the PV rooftop or façade installation and is reduced by EP filling at 10.3℃ and 11.57℃. The average module surface temperature in SH is increased from -0.71℃ to 0.31℃, showing a better snow melting potential for EP backfilling in cities with a relatively lower ambient temperature in Winter.

Table 7 Annual output results for two specific cases with air and EP filling

Parameter	Sum/Average (SH)	Sum/Average (HK)	Max/hr (SH)	Max/hr (HK)	Min/hr (SH)	Min/hr (HK)
Air filling						
E_{pv} (kWh/Wp)	1.010	1.075	0.696	0.716	-	-
T_c (℃)	20.69	26.70	57.83	64.86	-0.67	10.31
T_{sur} (℃)	19.23	25.14	49.51	55.12	-0.71	10.28
T_{road} (℃)	20.23	26.23	56.75	63.72	-1.00	10.11
EP filling						
E_{pv} (kWh/Wp)	1.012	1.078	0.700	0.720	-	-
T_c (℃)	19.80	25.82	47.53	53.29	1.13	11.76
T_{sur} (℃)	19.10	25.05	45.27	50.47	0.31	11.10
T_{road} (℃)	20.19	26.19	56.65	63.63	-1.10	10.05

Technically, the hourly performance of the PVP module EP backfilling and primary weather data are analyzed in two specific cities for an entire year, SH and HK, as presented in Fig. 16. The PV output is still determined by the solar irradiance to a large extent, making spring and summer months with higher PV potential. The variation of backfilling material from air to EP filling leads to the apparent reduction of T_{cell} and its yearly range, especially from May to Oct. and in the city with lower altitudes, HK. Likewise, the temperature variation range of T_{sur} is also reduced with EP filling, which has higher heat capacity and conductivity than air in heat conduction, decreasing summer T_{road} and increasing winter T_{road}. Furthermore, the maximum and minimum road and EP-filling module surface temperature gap could reach 12.37℃ (6278hr in Sep.) and -1.86℃ (8624hr in Dec.) for SH, and 13.24℃ (4527hr in Jul.) and -1.74℃ (583/584hr in Jan.) for HK respectively, showing the explicit effect on summer heat island alleviation and winter road snow melting effect.

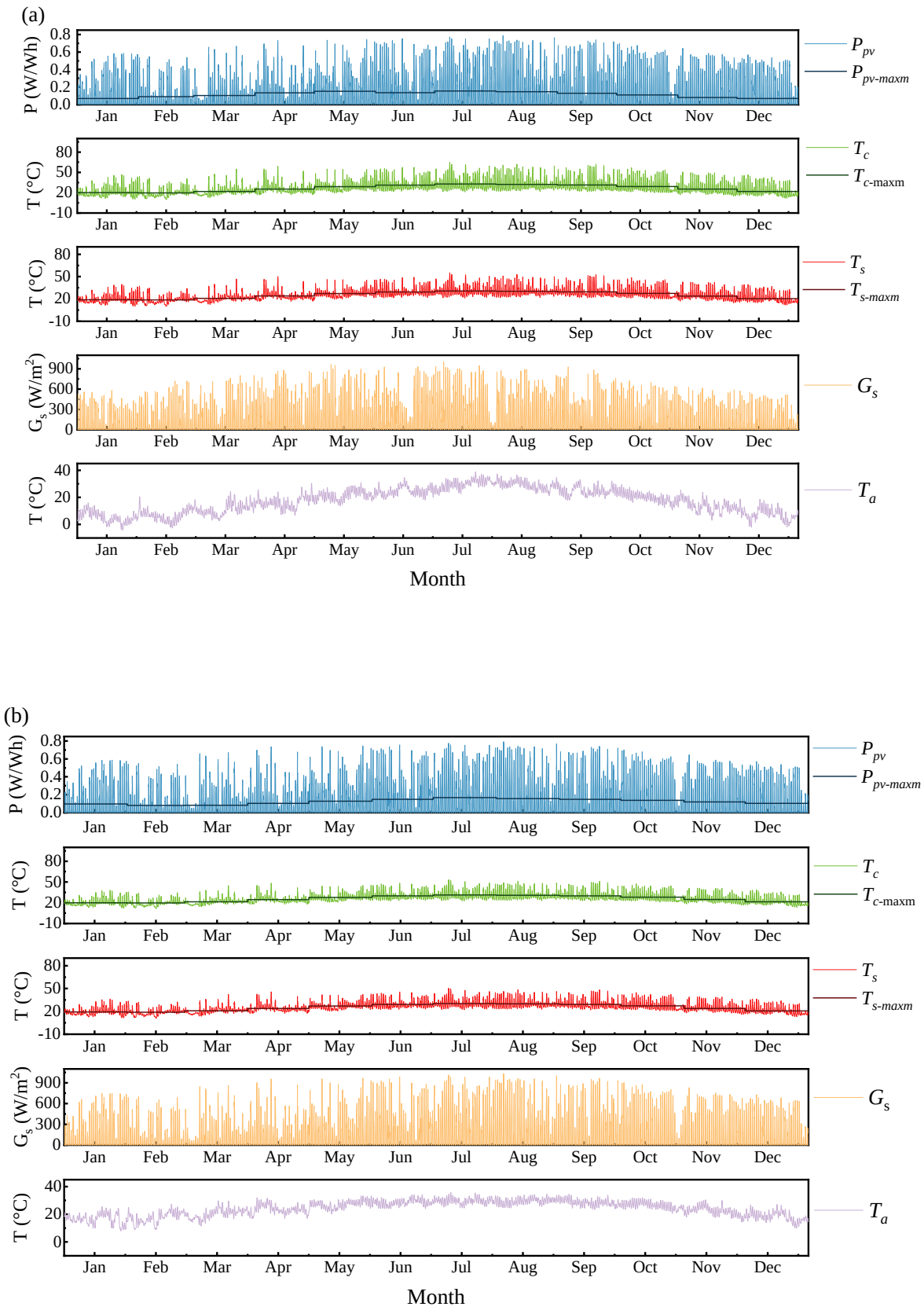

Fig. 16 Annual results: (a) module with EP filling in SH; (b) module with EP filling in HK.

5.3 Potential of PV road module in China

The PVP potential is another focus in academia in the near future [9]. The T_{ini} is selected as the annual average T_{amb} of the 256 cities in China. The global solar irradiance in China is displayed in Fig. 17 to reference the solar irradiance level. The seasonal variations of the different cities are presented in the following figures on seasonal values of temperature difference of T_{sur} and T_{road} (Fig. 18), PV cell temperature T_{cell} (Fig. 19), and PV output E_{pv} (Fig. 20).

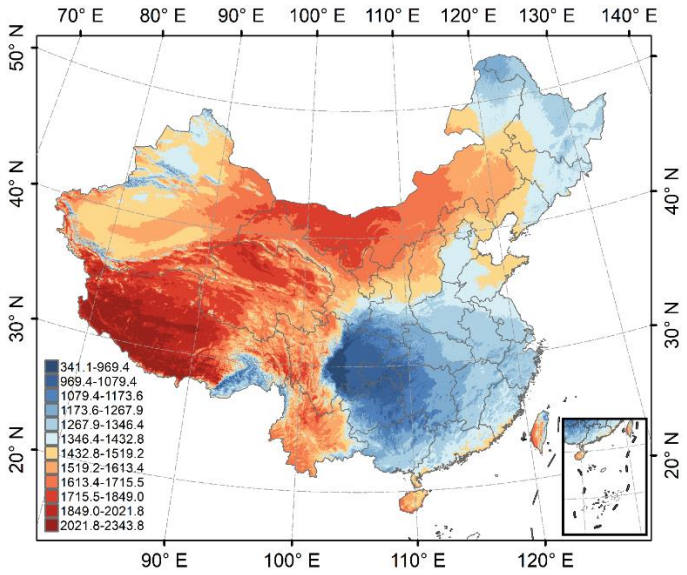

Fig. 17 Reference solar irradiance for China (unit: MJ/m^2, data from [66])

As shown in Fig. 18, in Summer and Spring, the selected cities in China all have achieved the heat island effect alleviation on the urban roadway, with the seasonal average road surface temperature reduction ranging from -1.37℃ to -4.18℃ (Jul. to Sep.) and from -1.03℃ to -4.36℃ (Apr. to Jun.). The heat island effect alleviation is influenced positively by both solar irradiance and ambient temperature of different cities to a large extent, with higher potential in northern and western cities in China. When it comes to Winter and Fall with relatively low solar irradiance and ambient temperature for the selected cities, the roadway surface temperature increases of PVP module compared to the conventional asphalt concrete roadway could be found in the majorities of the cities in northwest and east of China.

The maximum average temperature gap between T_{sur} and T_{road} at 0.40℃ in Fall and 0.47℃ in Winter, showing explicit snow melting capacity, especially for northern cities. Taking Beijing as an example, the maximum temperature is increased by using PVP instead of the conventional asphalt concrete road reaches 3.36℃ in Winter, while the average maximum temperature increase only appears to be 0.13℃.

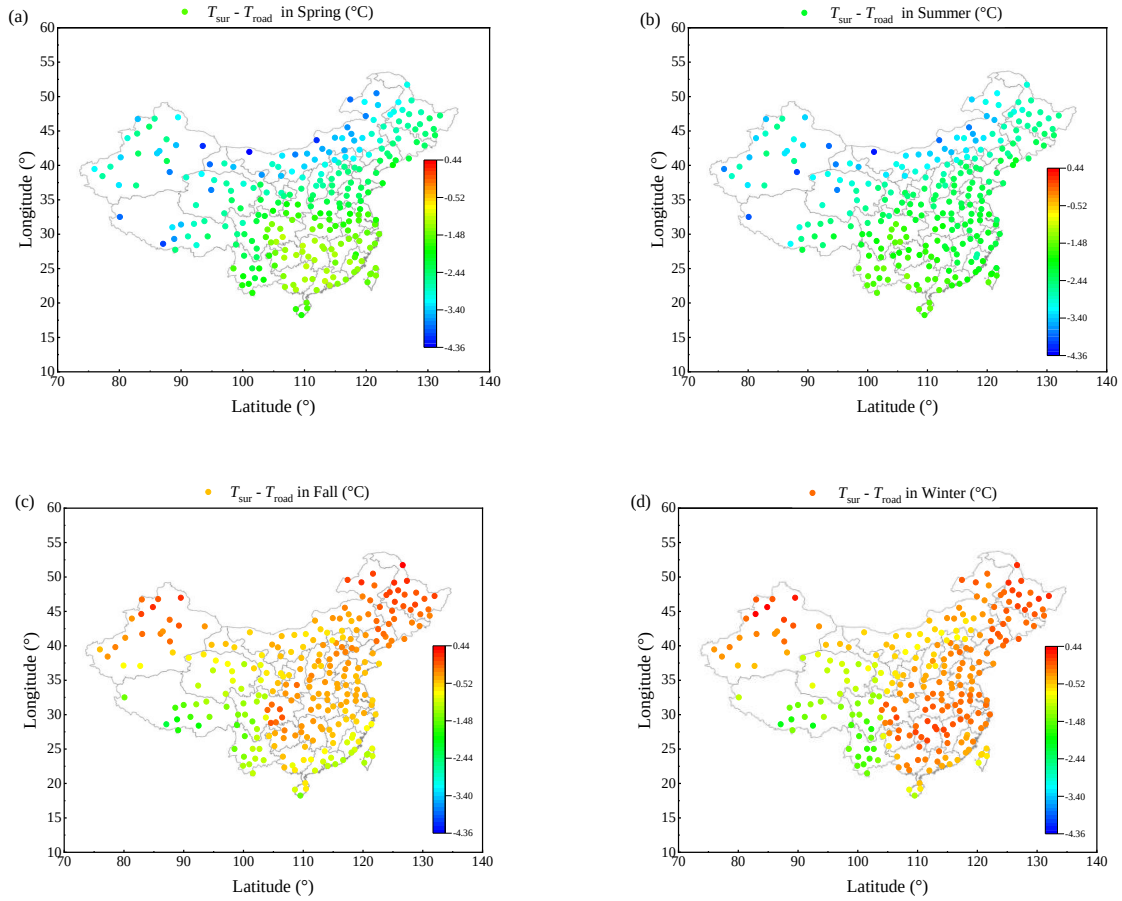

Fig. 18 Seasonal average heat island effect alleviation effect and snow melting potential of PV module surface in China: (a) Spring; (b) Summer; (c) Fall; (d) Winter.

Regarding the T_{cell} performance in Fig. 19, which is crucial to solar PV production, most cities have the average T_{cell} lower than 52℃ in Winter and Fall, especially for the northeast cities with extremely low ambient temperature. In Spring and Summer, the T_{cell} is still a challenge to PV output, with some cities' seasonal maximum T_{cell} over 52℃ in red and orange points located in southern, northern, and the center of China. The southwest Chinese cities have higher PV output potential for roadway applications, with high solar irradiance shown in Fig. 17 and low spring and summer time T_{cell} presented in Fig. 19 (a) and (b). Compared with the rooftop or façade PV with poorer heat dissipation conditions, the maximum T_{cell} in the selected Chinese cities, 61.05℃, is not a high PV cell temperature in practical use. Thus, the PVP is a good choice for PV installation increase in China, especially southwest zone of it.

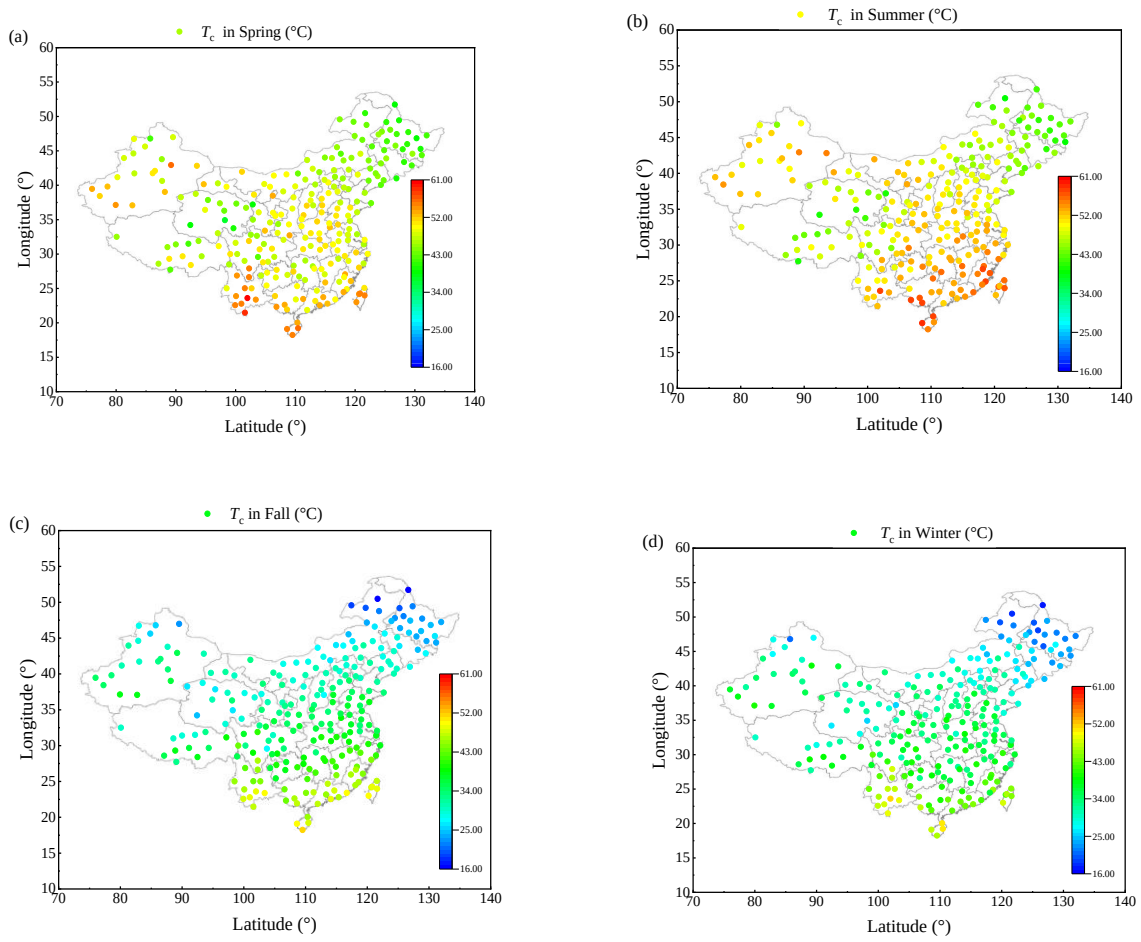

Fig. 19 Seasonal maximum T_{cell} in China: (a) Spring; (b) Summer; (c) Fall; (d) Winter.

The PV annual output potential of the PVP module in most of the Chinese cities is displayed in Fig. 20. The estimated annual PV generation potential of PVP system in the 255 Chinese cities ranges from 0.70 to 1.83 kWh/Wp. The southern China, especially southwest part, is strongly recommended, with most of the cities showing high PV generation potential over 1.38kWh/Wp. Regarding the energy consumption distribution with higher density in the east than the west, the east and south coastline cities in China, such as Hong Kong, are also recommended to increase the onsite renewable consumption, while several parts of south inland provinces are not so recommended, including Guizhou, Sichuan, Guangxi and Hunan provinces.

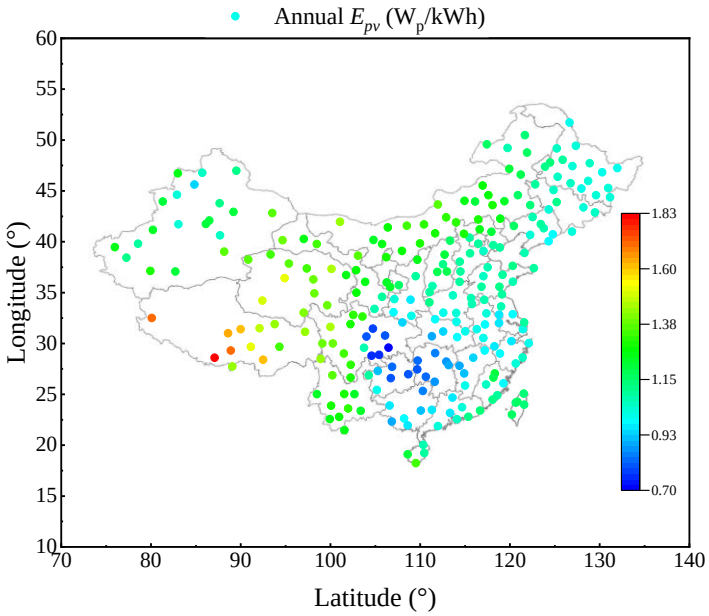

Fig. 20 Estimated annual PVP energy output in China

5.4 Economic discussion and limitations

The economic cost of the PVP may be a critical concern in future PVP manufacturing and investment, though it is still in the infant stage. According to the previous studies, the unit cost of different PVP modules varies from 400-800\$/m^2 for hollow structure with 34.9kWh annual output, 1500-2000\$/m^2 or higher for non-hollow structure with 53.4kWh annual output [20], 637CNY/m^2 with thin-film solar cell and self-compacting concrete [31], 481.86\$/m^2 for highway [30], to 116\$/kWh for zebra crossing box with 5.7kWh output [45]. Although the costs in the previous studies are relatively high, the cost of PVP module is decreasing with the PV cost reduction. In this study, the total cost of the prefabricated module is approximately 1509\$/m^2 or 12\$/Wp for a small road, including the manufacturing, freight and corporate profit. The cost considered at this period is the commercial trading cots with customized panels in small amount. Based on our previous study on levelized cost of energy (LCOE) calculation [58], if taking Hong Kong as an example, the LCOE on the power generation side of the EP backfilling PVP module could approximately reaches 1.2\$/kWh during its 10-year lifetime. Although the feed-in tariff in Hong Kong could reach 4hkd/kWh, the revenue could still not cover the cost at this stage [67]. However, it should be mentioned that the marginal manufacturing cost will be sharply decreased if the PVP modules are ordered in large amount and the revenues could be even higher with the introduction of carbon trading. Also, the modular design for the PVP module could reduce the replacement cost and ease the installation/replacement process.

Besides the relatively high investment for the PVP module, the installation condition on the roadways also brings about higher energy loss during PV generation and may increase the operation and maintenance cost of the pavement module. Thus, more relative studies are expected in future, including the structure analyses for longer lifetime, road surface design both for anti-slipping feature and dust removing, and addition of water/air pipes to decrease cell temperature for higher electricity efficiency. Although PVP module may have a less capacity factor compared to the conventional PV roof, it could make good use of the roadway space and add to the urban onsite renewable generation.

As for the system design for the PVP module application, such as battery/grid connection and PV array design, is out of the scope of this study. Several perspectives will be conducted in the future study, including battery capacity sizing, PV array topology design with partial shading consideration, and smart operation strategy for the energy community concerning both energy and vehicle flows.

6 Conclusions

Under the carbon neutrality targets, photovoltaic (PV) installation is expected to increase further in the near future. Due to the limited urban area and low road use rate, harvesting solar energy from road is a novel trend which is suitable for practical use. However, the PV generation and road temperature estimation are not accurate enough based on the conventional PV generation model and heat transfer model in previous studies without appropriate consideration of ground heat transfer.

This study proposes a thermal-electrical model for PV pavement (PVP) module technical performance, including PV output, PV cell, and module surface temperature, and the surrounding road temperature. The two-dimensional heat nodal model is established based on the alternative direction finite difference method. The heat and 5-parameter PV electrical models are connected via the PV cell energy balance. The grid independence test is conducted, and 6000 grid number is selected. The proposed mathematical model is verified based on the outdoor test on a sunny day in Hong Kong, with mean absolute error at 1.68% and 3.60% for PV cell temperature and PV output, respectively.

Besides the simulation model establishment, several experiments are conducted in lab and outdoor environments. The PV model's crucial parameters are tested based on the lab test for the 31.5Wp prefabricated PVP module. Also, the PV module current and voltage curves under different solar irradiance are displayed. Moreover, the PV output on a sunny day could reach 0.68 kWh/m^2, with PV generation efficiency at 14.7%. Besides, the anti-skid road surface property has also experimented, and results show better performance with mean British Pendulum Number at 92.8-114.6 under dry condition and 48.8 under wet condition, compared to the previous solar pavement test.

Based on the established thermal-electrical model simulation, the parametric analyses on surrounding ground material and backfilling of the PVP module are conducted. Results show that the asphalt concrete road surface brings about higher road surface and PVP module surface temperature variation compared to cement, e.g., at 11.28℃ for asphalt concrete and 9.46℃ in typical summer days for Hong Kong. The backfilling material change from air to epoxy resin sharply reduces the heat island alleviation effect in both Shanghai and Hong Kong.

Moreover, the annual performance of the PVP modules for Shanghai and Hong Kong is compared with air and epoxy resin filling. The epoxy resin filling reduces the annual maximum PVP module surface temperature by 8.6% (Shanghai) and 8.4% (Hong Kong), which could also increase the minimum surface temperature by 1.02℃ (Shanghai) and 1.48℃ (Hong Kong), showing both obvious heat island alleviation and snow melting potential in different seasons. The average heat island effect alleviation could reach 13.16℃ for Hong Kong and 11.38℃ for Shanghai, with annual PV output at approximately 1.08 and 1.01kWh/Wp, respectively. Furthermore, the annual output potential of the PVP module is simulated for 255 Chinese cities, and the seasonal variation in heat performance is discussed. The heat island effect alleviation and snow melting capacity could be found via the seasonal average results, e.g., average road surface temperature reduction range from -1.37℃ to -4.18℃ in summer and maximum increase range at 0.47℃ in Winter. The annual PVP system

electricity potential ranges from 0.70 to 1.83 kWh/Wp, with the cities in the west and northeast China showing higher PV generation potential.

Acknowledgements

The authors would like to appreciate the financial support from the Hong Kong PhD Fellowship Scheme (HKPFS) and the Research Impact Fund (No.: R5007-18) of the Research Grant Council of the Hong Kong SAR Government. Appreciation also goes to Dr. Zhongshi Li from Shenzhen Huitong Photoelectric Co. LTD for module manufacturing.

Appendix

(1) Thermal nodal equations of the PVP module

The nodal equations at (0, 0<y) can be displayed as follows:

$$\begin{aligned}\left(1+N_{1,li}\right)T_{gd}^{p+1}(0,j)-N_{1,li}T_{gd}^{p+1}(1,j)=\left(1-N_{2,li}\right)T_{gd}^{p}(0,j)\\ +0.5N_{2,li}T_{gd}^{p}(0,j-1)+0.5N_{2,li}T_{gd}^{p}(0,j+1)\end{aligned} \quad (1)$$

$$\begin{aligned}\left(1+N_{2,li}\right)T_{gd}^{p+1}(0,j)-0.5N_{2,li}T_{gd}^{p+1}(0,j-1)-0.5N_{2,li}T_{gd}^{p+1}(0,j+1)=\\ \left(1-N_{1,li}\right)T_{gd}^{p}(0,j)+N_{1,li}T_{gd}^{p}(1,j)\end{aligned} \quad (2)$$

The nodal equations for the surface of ground (0<x<m_i, 0) are shown as:

$$\begin{aligned}\left(1+N_{1,l1}\right)T_{gd}^{p+1}(i,0)-0.5N_{1,l1}T_{gd}^{p+1}(i+1,0)-0.5N_{1,l1}T_{gd}^{p+1}(i-1,0)=\\ \left(1-N_{2,l1}\right)T_{gd}^{p}(i,0)+N_{2,l1}T_{gd}^{p}(i,1)+N_hQ_{gd}\end{aligned} \quad (3)$$

$$\begin{aligned}\left(1+N_{2,l1}\right)T_{gd}^{p+1}(i,0)-N_{2,l1}T_{gd}^{p}(i,1)-N_hQ_{gd}=\\ \left(1-N_{1,l1}\right)T_{gd}^{p}(i,0)+0.5N_{1,l1}T_{gd}^{p}(i+1,0)+0.5N_{1,l1}T_{gd}^{p}(i-1,0)\end{aligned} \quad (4)$$

The nodal equations inside the different ground layers *li*, (l_1 l_2 l_3 (0<x<m_i, 0<y) could be expressed as follows:

$$\begin{aligned}\left(1+N_{1,li}\right)T_{gd}^{p+1}(i,j)-0.5N_{1,li}T_{gd}^{p+1}(i+1,j)-0.5N_{1,li}T_{gd}^{p+1}(i-1,j)=\\ \left(1-N_{2,li}\right)T_{gd}^{p}(i,j)\ +0.5N_{2,li}T_{gd}^{p}(i,j+1)+0.5N_{2,li}T_{gd}^{p}(i,j-1)\end{aligned} \quad (5)$$

$$\begin{aligned}\left(1+N_{2,li}\right)T_{gd}^{p+1}(i,j)-0.5N_{2,li}T_{gd}^{p+1}(i,j+1)-0.5N_{2,li}T_{gd}^{p+1}(i,j-1)=\\ \left(1-N_{1,li}\right)T_{gd}^{p}(i,j)+0.5N_{1,li}T_{gd}^{p}(i+1,j)+0.5N_{1,li}T_{gd}^{p}(i-1,j)\end{aligned} \quad (6)$$

The energy balance of PV module surface (m_i<x<e_i, 0) can be displayed as:

$$\begin{aligned}\left(1+N_{1,pv}\right)T_{pvs}^{p+1}(i,0)-0.5N_{1,pv}T_{pvs}^{p+1}(i+1,0)-0.5N_{1,pv}T_{pvs}^{p+1}(i-1,0)=\\ \left(1-N_{2,pv}\right)T_{pvs}^{p}(i,0)+N_{2,pv}T_{cell}^{p}(i,1)+N_hQ_{pvs}\end{aligned} \quad (7)$$

$$\begin{aligned}&\left(1+N_{2,pv}\right)T_{pvs}^{p+1}(i,0)-N_{2,pv}T_{cell}^{p}(i,1)-N_hQ_{pvs}=\\&\left(1-N_{1,pv}\right)T_{pvs}^{p}(i,0)+0.5N_{1,pv}T_{pvs}^{p}(i+1,0)+0.5N_{1,pv}T_{pvs}^{p}(i-1,0)\end{aligned}\quad(8)$$

The equations for the PV cell layer ($m_i<x<e_i$, 1) are expressed below:

$$\begin{aligned}&\left(1+N_{1,pv}\right)T_{cell}^{p+1}(i,1)-0.5N_{1,pv}T_{cell}^{p+1}(i+1,1)-0.5N_{1,pv}T_{cell}^{p+1}(i-1,1)=\\&\left(1-N_{2,pv}\right)T_{cell}^{p}(i,1)+0.5N_{2,pv}T_{cell}^{p}(i,0)+0.5N_{2,pv-l1}T_{gd}^{p}\left(i,m_{1j}\right)+N_hQ_{cell}\end{aligned}\quad(9)$$

$$\begin{aligned}&\left(1+N_{2,pv}\right)T_{cell}^{p+1}(i,1)-0.5N_{2,pv}T_{cell}^{p}(i,0)-0.5N_{2,pv-l1}T_{gd}^{p}\left(i,m_{1j}\right)-N_hQ_{cell}=\\&\left(1-N_{1,pv}\right)T_{cell}^{p}(i,0)+0.5N_{1,pv}T_{cell}^{p}(i+1,0)+0.5N_{1,pv}T_{cell}^{p}(i-1,0)\end{aligned}\quad(10)$$

The boundary of PV module surface (e_i, 0) is displayed as follows:

$$\begin{aligned}&\left(1+N_{1,pv}\right)T_{pvs}^{p+1}(e_i,0)-N_{1,pv}T_{pvs}^{p+1}(e_i-1,0)=\\&\left(1-N_{2,pv}\right)T_{pvs}^{p}(e_i,0)+N_{2,pv}T_{pvs}^{p}(e_i,1)+N_hQ_{pvs}\end{aligned}\quad(11)$$

$$\begin{aligned}&\left(1+N_{2,pv}\right)T_{pvs}^{p+1}(e_i,0)-N_{2,pv}T_{pvs}^{p+1}(e_i,1)=\\&\left(1-N_{1,pv}\right)T_{pvs}^{p}(e_i,0)+N_{1,pv}T_{pvs}^{p}(e_i+1,0)-N_hQ_{pvs}\end{aligned}\quad(12)$$

Likewise, the boundary of the PV cell layer (e_i, 1) could be expressed in the following equations:

$$\begin{aligned}&\left(1+N_{1,pv}\right)T_{cell}^{p+1}(e_i,1)-N_{1,pv}T_{pvs}^{p+1}(e_i-1,0)=\\&\left(1-N_{2,pv}\right)T_{cell}^{p}(e_i,1)+0.5N_{2,pv}T_{pvs}^{p}(e_i,0)\\&+0.5N_{2,pv-l1}T_{gd}^{p}\left(e_i,m_{1j}\right)+N_hQ_{cell}\end{aligned}\quad(13)$$

$$\begin{aligned}&\left(1+N_{2,pv}\right)T_{cell}^{p+1}(e_i,1)-0.5N_{2,pv}T_{pvs}^{p+1}(e_i,0)-0.5N_{2,pv-l1}T_{gd}^{p+1}\left(e_i,m_{1j}\right)=\\&\left(1-N_{1,pv}\right)T_{cell}^{p}(e_i,1)+N_{1,pv}T_{cell}^{p}(e_i+1,1)-N_hQ_{cell}\end{aligned}\quad(14)$$

The equations of the interface between two adjacent layers (named as m and n) are shown as follows:

$$\begin{aligned}&\left(1+N_{1,lm-n}\right)T_{gd}^{p+1}(i,j)-0.5N_{1,lm-n}T_{gd}^{p+1}(i+1,j)\\&-0.5N_{1,lm-n}T_{gd}^{p+1}(i-1,j)=\left(1-N_{2,lm-n}\right)T_{gd}^{p}(i,j)\\&+0.5N_{2,lm-n}T_{gd}^{p}(i,j+1)+0.5N_{2,lm-n}T_{gd}^{p}(i,j-1)\end{aligned}\quad(15)$$

$$\begin{aligned}&\left(1+N_{2,lm-n}\right)T_{gd}^{p+1}(i,j)-0.5N_{2,lm-n}T_{gd}^{p+1}(i,j+1)\\&-0.5N_{2,lm-n}T_{gd}^{p+1}(i,j-1)=\left(1-N_{1,lm-n}\right)T_{gd}^{p}(i,j)\\&+0.5N_{1,lm-n}T_{gd}^{p}(i+1,j)+0.5N_{1,lm-n}T_{gd}^{p}(i-1,j)\end{aligned}\quad(16)$$

(2) Dusting influence on the PVP module during lab test

The influence of dust, soiling or other dirty is a common concern to PVP module, and may lead to approximately 3%/year PV output decrease in Poland during real operation and maximum daily efficiency loss for Hong Kong is estimated to be within 0.2% [68]. To clearly display the influence of dusting/soiling on PV degradation, the prefabricated PVP module is tested under high and medium solar irradiances with three different dusting levels, none, slight and severe. The power outputs with ideal PV output under the same solar irradiance and cell temperature situations are compared in Fig. 21. Although the severe dusting may decrease the PV output by 55% under 1000W/m^2 solar irradiance and 42.9℃ PV cell temperature, the situation could hardly appear and it still generated the electricity. The slight dusting is more common and are measured with 11.9% and 7.6% PV output reduction under high and medium solar irradiance, only 10.1% and 6.6% higher than measured PV output with normal wire losses.

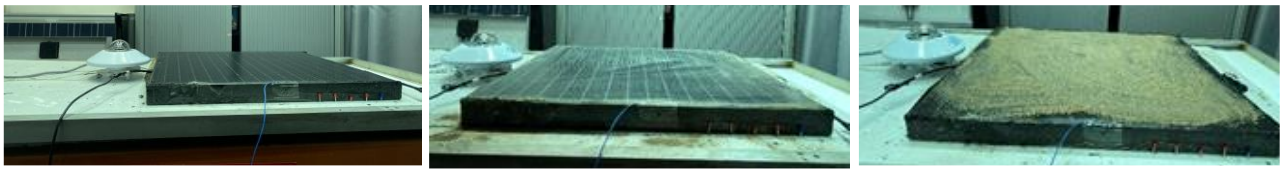

(a) (b) (c)

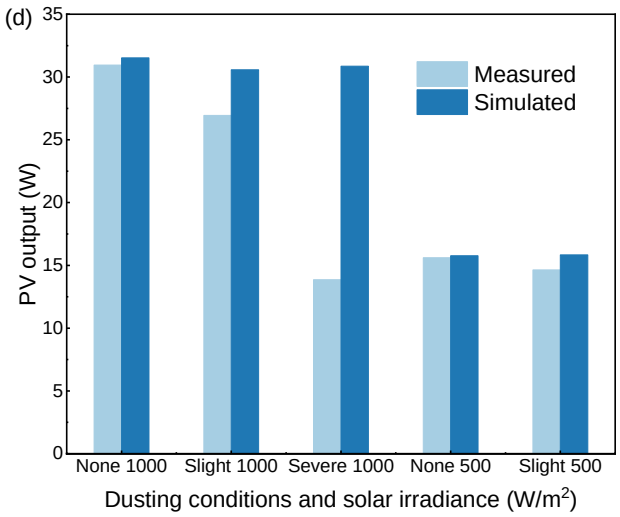

Fig. 21 Dusting influence under different solar irradiances: (a) PVP module without dust; (b) PVP module with slight dust; (c) PVP module with severe dust; (d) PV output degradation comparison.

References

[1] Chen S, Lu X, Miao Y, Deng Y, Nielsen CP, Elbot N, et al. The Potential of Photovoltaics to Power the Belt and Road Initiative. Joule. 2019;3:1895-912.

[2] Comello S, Reichelstein S, Sahoo A. The road ahead for solar PV power. Renewable and Sustainable Energy Reviews 2018;92:744-56.
[3] Zhang Y, Ma T, Yang H. Grid-connected photovoltaic battery systems: A comprehensive review and perspectives. Applied Energy. 2022;328:120182.
[4] IRENA. Renewable capacity statistics 2022. Abu Dhabi: The International Renewable Energy Agency; 2022.
[5] Hong Kong's CLIMATE ACTION PLAN 2050. Hong Kong: Hong Kong SAR; 2021.
[6] China MoTotPsRo. 2021 China Transport Industry Development Statistical Bulletin. 2022.
[7] Efthymiou C, Santamouris M, Kolokotsa D, Koras A. Development and testing of photovoltaic pavement for heat island mitigation. Solar Energy. 2016;130:148160.
[8] Duman AC, Güler Ö. Techno-economic analysis of off-grid photovoltaic LED road lighting systems: A case study for northern, central and southern regions of Turkey. Building and Environment. 2019;156:89-98.
[9] Ferri C, Ziar H, Nguyen TT, Lint Hv, Zeman M, Isabella O. Mapping the photovoltaic potential of the roads including the effect of traffic. Renewable Energy. 2022;182:427-42.
[10] Zhou B, Pei J, Calautit JK, Zhang J, Guo F. Solar self-powered wireless charging pavement— a review on photovoltaic pavement and wireless charging for electric vehicles. Sustainable Energy & Fuels. 2021;5:5139-59.
[11] Chu L, Zhai S, Ahmad W, Zhang J, Zang Y, Yan W, et al. High-performance large-area perovskite photovoltaic modules. Nano Research Energy. 2022;1:9120024.
[12] Zeng J, Bi L, Cheng Y, Xu B, Jen AK-Y. Self-assembled monolayer enabling improved buried interfaces in blade-coated perovskite solar cells for high efficiency and stability. Nano Research Energy. 2022;1:e9120004.
[13] Wei J, Xiao J, Yuan D, Lu H, Xu S, Huang Y. Design and experiment of thermoelectric asphalt pavements with power-generation and temperature-reduction functions. Energy & Buildings. 2018;169:39-47.
[14] Xie P, Wang H. Potential benefit of photovoltaic pavement for mitigation of urban heat island effect. Applied Thermal Engineering 2021;191:116883.
[15] Hamakareem MI. Solar Roadways: Purpose, Construction, and Applications. The Constructor.
[16] Sun W, Lu G, Ye C, Chen S, Hou Y, Wang D, et al. The State of the Art: Application of Green Technology in Sustainable Pavement. Advances in Materials Science and Engineering. 2018;2018:9760464.
[17] Nussbaum JH, Lake RA, Coutu RA. Standardized Testing of Non-Standard Photovoltaic Pavement Surfaces. IEEE. 2016:1-8.
[18] Golden JS, Carlson J, Kaloush KE, Phelan P. A comparative study of the thermal and radiative impacts of photovoltaic canopies on pavement surface temperatures. Solar Energy. 2007;81:872-83.
[19] JIANG H-f, CEN Y-q, ZHA X-d, ZHANG Q-s. Current Situation and Development Trend of Solar Pavement Technology. 2nd International Conference on Energy and Power Engineering (EPE 2018)2018. p. 1-7.
[20] Hu H, Vizzari D, Zha X, Roberts R. Solar pavements: A critical review. Renewable and Sustainable Energy Reviews 2021;152:111712.
[21] Dezfooli AS, Nejad FM, Zakeri H, Kazemifard S. Solar pavement: A new emerging technology. Solar Energy 2017;149:272-84.
[22] Channi HK. Solar Pavement: Smart Means of Transportation. International Journal of Management, IT & Engineering. 2019;9:211-7.
[23] Klimenta D, Jevti M, Andriukaitis D, Mijailovi V. Increasing the transmission performance of a conventional 110 kV cable line by combining a hydronic concrete pavement system with photovoltaic floor tiles. Electrical Engineering. 2021;103:1401-15.
[24] Pei J, Zhou B, Lyu L. e-Road: The largest energy supply of the future? Applied Energy. 2019;241:174-83.

[25] Patila AR, Khairnara VY, Kokatea DAV, Narkhede DRS. A Novel Route for Construction of Smart Highways by Using Photovoltaic Solar Panels. International Journal of Research and Analytical Reviews. 2018;5:491-6.
[26] Ma T, Yang H, Gu W, Li Z, Yan S. Development of walkable photovoltaic floor tiles used for pavement. Energy Conversion and Management. 2019;183:764-71.
[27] Li S, Gu W, Liu X, Zhou Y, Chen Z, Zhang X, et al. Pavement integrated photovoltaic thermal (PIPVT) system: A temporal and spatial analysis of energy and exergy performance. Journal of Cleaner Production. 2022;340:130782.
[28] Duarte F, Ferreira A. Energy harvesting on road pavements: state of the art. Proceedings of the Institution of Civel Engineers. 2016;169:79-90.
[29] Wang J, Xiao F, Zhao H. Thermoelectric, piezoelectric and photovoltaic harvesting technologies for pavement engineering. Renewable and Sustainable Energy Reviews 2021;151:111522.
[30] Vizzari D, Gennesseaux E, Lavaud S, Bouron S, Chailleux E. Pavement energy harvesting technologies: a critical review. RILEM Technical Letters. 2021;6:93-104.
[31] Zha X, Qiu M, Hu H, Hu J, Lv R, Pan Q. Simulation of structure and power generation for Self-Compacting concrete hollow slab solar pavement with micro photovoltaic array. Sustainable Energy Technologies and Assessments. 2022;53:102798.
[32] Li S, Chen Z, Liu X, Zhang X, Zhou Y, Gu W, et al. Numerical simulation of a novel pavement integrated photovoltaic thermal (PIPVT) module. Applied Energy. 2021;283:116287.
[33] Ma T, Li S, Gu W, Weng S, Peng J, Xiao G. Solar energy harvesting pavements on the road: comparative study and performance assessment. Sustainable Cities and Society. 2022;81:103868.
[34] Xiang B, Yuan Y, Ji Y, Cao X, Zhou J. Thermal and electrical performance of a novel photovoltaic-thermal road. Solar Energy. 2020;199:1-18.
[35] Xiang B, Ji Y, Yuan Y, Wu D, Zeng C, Zhou J. 10-year simulation of photovoltaic-thermal road assisted ground source heat pump system for accommodation building heating in expressway service area. Solar Energy. 2021;215:459-72.
[36] Xiang B, Ji Y, Yuan Y, Zeng C, Cao X, Zhou J. Performance analysis of photovoltaic-thermal road assisted ground source heat pump system during non-heating season. Solar Energy. 2021;221:10-29.
[37] Zhou B, Pei J, Calautit JK, Zhang J, Yong LX, Pantua CAJ. Analysis of mechanical response and energy efficiency of a pavement integrated photovoltaic/thermal system (PIPVT). Renewable Energy. 2022;194:1-12.
[38] Zhou B, Pei J, Hughes BR, Nasir DS, Zhang J. Analysis of mechanical properties for two different structures of photovoltaic pavement unit block. Construction and Building Materials 2020;239:117864.
[39] Zhou B, Pei J, Nasir DM, Zhang J. A review on solar pavement and photovoltaic/thermal (PV/T) system. Transportation Research Part D. 2021;93:102753.
[40] López-Escalante MC, Fernández-Rodríguez M, Caballero LJ, Martín F, Gabás M, Ramos-Barrado JR. Novel encapsulant architecture on the road to photovoltaic module power output increase. Applied Energy 2018;228:1901-10.
[41] Papadimitriou CN, Psomopoulos CS, Kehagia F. A review on the latest trend of Solar Pavements in Urban. Technologies and Materials for Renewable Energy, Environment and Sustainability, TMREES18. Athens, Greece2018.
[42] He H, Li S, Wang S, Li B, Ma Z, Jie, Fei L. Investment strategies under stochastic electricity prices and implications for charging infrastructure network coverage: A case ofphotovoltaic pavements. Computers & Industrial Engineering. 2022;172:108523.
[43] Hu M, Song X, Bao Z, Liu Z, Wei M, Huang Y. Evaluation of the Economic Potential of Photovoltaic Power Generation in Road Spaces. Energies. 2022;15:6408.
[44] Jiang W, Yuan D, Xu S, Hu H, Xiao J, Sha A, et al. Energy harvesting from asphalt pavement using thermoelectric technology. Applied Energy. 2017;205:941-50.
[45] Hossain MFT, Dessouky S, Biten AB, Montoya A, Fernandez D. Harvesting Solar Energy from Asphalt Pavement. Sustainability. 2021;13:12807.

[46] Ma T, Yang H, Lu L. Solar photovoltaic system modeling and performance prediction. Renewable & Sustainable Energy Reviews. 2014;36:304-15.
[47] Gu W, Ma T, Shen L, Li M, Zhang Y, Zhang W. Coupled electrical-thermal modelling of photovoltaic modules under dynamic conditions. Energy. 2019;188:116043.
[48] Soto WD, Klein SA, Beckman WA. Improvement and validation of a model for photovoltaic array performance. Solar Energy. 2006;80:78-88.
[49] Tian H, Mancilla-David F, Ellis K, Muljadi E, Jenkins P. A cell-to-module-to-array detailed model for photovoltaic panels. Solar Energy 2012;86:2695-706.
[50] Petrone G, Spagnuolo G, Vitelli M. Analytical model of mismatched photovoltaic fields by means of Lambert W-function. Solar Energy Materials & Solar Cells. 2007;91:1652-7.
[51] Ma T, Gu W, Shen L, Li M. An improved and comprehensive mathematical model for solar photovoltaic modules under real operating conditions. Solar Energy. 2019;184:292-304.
[52] Gu W, Ma T, Li M, Shen L, Zhang Y. A coupled optical-electrical-thermal model of the bifacial photovoltaic module. Applied Energy. 2020;258:114075.
[53] Xinyi F, Ma T. Solar photovoltaic system under partial shading and perspectives on maximum utilization of the shaded land. International Journal of Green Energy. 2023;23:378-89.
[54] Bai J, Cao Y, Hao Y, Zhang Z, Liu S, Cao F. Characteristic output of PV systems under partial shading or mismatch conditions. Solar Energy 2015;112:41-54.
[55] Zhou K, Mao J, Li Y, Hua Z. Comparative study on thermal performance of horizontal ground source heat pump systems with Dirichlet and Robin boundary conditions on ground surface. Energy Conversion and Management. 2020;225:113469.
[56] Nam Y, Ooka R, Hwang S. Development of a numerical model to predict heat exchange rates for a ground-source heat pump system. Energy and Buildings 2008;40:2133-40.
[57] Wong LT, Chow WK. Solar radiation model. Applied Energy. 2001;69:191-224.
[58] Zhang Y, Ma T, Elia Campana P, Yamaguchi Y, Dai Y. A techno-economic sizing method for grid-connected household photovoltaic battery systems. Applied Energy. 2020;269:115106.
[59] Mermoud A, Villoz M, Wittmer B, Oliosi M, Pepoli S, Lang N, et al. PVSYST PHOTOVOLTAIC SOFTWARE TUTORIAL. Switzerland2022.
[60] Ma T, Yang H, Gu W, Li Z, Yan S. Development of walkable photovoltaic floor tiles used for pavement. Energy Conversion and Management 2019;183:764-71.
[61] Ma T, Li M, Kazemian A. Photovoltaic thermal module and solar thermal collector connected in series to produce electricity and high-grade heat simultaneously. Applied Energy. 2020;261:114380.
[62] CIZMECIOGLU M, GUPTA A, FEDORS RF. Influence of Cure Conditions on Glass Transition Temperature and Density of an Epoxy Resin. Journal of Applied Polymer Science. 1986;32:6177-90.
[63] Standard Test Method for Measuring Surface Frictional Properties Using the British Pendulum Teste. In: ASTM, editor. PA 19428-2959. 100 Barr Harbor Drive, United States1998.
[64] T.N. Standard test procedure for measurement of skid resistance using the british pendulum tester. Zealand: Transit New Zealand Specification TNZ T/2.; 2000.
[65] Xu H, Shi H, Tan Y, Ye Q, Liu X. Modeling and assessment of operation economic benefits for hydronic snow melting pavement system. Applied Energy. 2022;326:119977.
[66] SOLARGIS. Download solar resource maps and GIS data for 200+ countries and regions. 2022.
[67] Feed-in Tariff Scheme in Hong Kong. HK Electric; 2019.
[68] Klugmann-Radziemska E. Degradation of electrical performance of a crystalline photovoltaic module due to dust deposition in northern Poland. Renewable Energy. 2015;78:418-26.